

PARTICLE MANIPULATION BY ATTRACTIVE AND REPULSIVE FORCES IN 2-D
STREAMING FLOWS

BY

DAVID VIJAY RAJU

THESIS

Submitted in partial fulfillment of the requirements
for the degree of Master of Science in Mechanical Engineering
in the Graduate College of the
University of Illinois at Urbana-Champaign, 2018

Urbana, Illinois

Adviser:

Professor Sascha Hilgenfeldt

ABSTRACT

In this piece of work, we have attempted to study the variation in the trajectory of microparticles as they move in flows which are characterized by the superposition of microbubble streaming and transport flows. Our experimental setup uses steady streaming flow generated by ultrasonically driven semi-cylindrical microbubble combined with Poiseuille flow. Previous experiments have shown instances of particles being repelled from the surface of the interface. Theoretical predictions suggest that particles that are not density matched may experience attractive forces which may cause them to be attracted toward the surface of the interface.

We can modify the previous experiments by lowering the strength of the streaming flow which allows for a relatively larger variety of particle trajectories. Experiments are conducted to study the effect of density mismatch, particle size and fluid viscosity. In this work, we also emphasize the importance of a new parameter which is the minimum surface to surface distance between the particle and the interface (quantity denoted by h_{min}).

In order to see the net effect of these forces on a microparticle we utilize a method that uses a few small particle trajectories to interpolate the entire flow field, which is then used to see the relative behavior of a particle.

We also comment on the development of asymptotic solutions to the Maxey Riley equations which allow us to predict the experimental behavior of a particle. We develop both a purely radial version which assists in making qualitative predictions as well as a 2-D analog which provides quantitative estimates of particle behavior in experiments.

We see a number of novel results from these experiments. Firstly, we show conclusive evidence of the presence of attractive forces on micro-particles in this flow field. Secondly, we show that the key parameter in the determination of the nature of the net force on the particle i.e. attraction vs repulsion is the value of h_{min} . Finally, we show that there is a very systematic way in which the attractive behavior varies with h_{min} , density mismatch and particle size. As a general rule it is seen that attractive behavior is most apparent in large particles which are denser than the fluid and have a value of h_{min} which is of the order of particle radius. It is seen that these results are qualitatively and semi-quantitatively consistent with the predictions obtained from both the purely radial and 2-D versions of the developed theory.

ACKNOWLEDGEMENTS

First and foremost, I would like to express my gratitude to my research advisor, Professor Sascha Hilgenfeldt, whose expert advice and guidance made this work possible. I am particularly grateful for his willingness to allow me the freedom to experiment and to explore different directions while working under him.

Special thanks go to Bhargav Rallabandi and Siddhansh Agarwal, whose theoretical work helped greatly in guiding my own project, and to Thameem Raqeeb, whose initial training and advice ensured my smooth transition into this research group. I also wish to thank the other group members and friends I have worked with Sangwoo Kim and Yichuan Li for helping make my time here more fruitful and enjoyable.

Finally, my warmest thanks go to my family for their unfailing and unconditional love and support.

TABLE OF CONTENTS

CHAPTER 1: INTRODUCTION	1
CHAPTER 2: EXPERIMENTAL SETUP	10
CHAPTER 3: THEORY	15
CHAPTER 4: EXPERIMENTAL RESULTS	27
CHAPTER 5: CONCLUSION	43
REFERENCES	46

CHAPTER 1: INTRODUCTION

1.1 INTRODUCTION

An increasingly popular technique in microfluidics is the actuation of micron-size bubbles to drive useful flows. The mechanism of interest here is known as acoustic steady streaming. Acoustic excitation of a microbubble causes it to undergo shape and volume oscillations that drive strong oscillatory flows which result in second-order steady streaming flows in the bulk of the medium [1–3].

Such bubbles have been variously used for practical applications such as particle trapping and sorting [4, 5], microfluidic mixing [6–8] and cell deformation and lysis [9], among others.

Among the many strengths of using bubbles as flow actuators is ease of manufacture using lithography techniques the addition of stationary bubbles to microfluidic devices requires only slight modifications to channel design. Previous work has provided detailed theoretical asymptotic descriptions of bubble streaming flows [7, 9, 18], as well as an overview of their applications towards trapping and focusing particles [3, 4].

We expand upon the previous work in [18] by looking at new behaviors of the particles and how it varies not only based on particle size but also based on experimentally controlled parameters density mismatch between particle and suspended fluid, and properties of the particle trajectory. First, we look at the description of a streaming flow followed by the superposition of a Poiseuille flow which is used in experiments. After this we look at a summary of the previous work followed by a short description of how we build on it.

1.2 STREAMING FLOW

The signal supplied to a piezoelectric transducer drives a periodic pressure variation in the fluid at the driving f . The oscillation of the piezo transducer causes the bubble to oscillate in

many different modes. As the bubbles are compressible, pressure variation causes the bubble surface to oscillate in the ‘breathing’ mode at the driving frequency f . The restorative surface tension force also causes the bubble to oscillate in a number of ‘shape’ modes as shown in [10]. It is seen that the ‘breathing’ mode is the dominant one and that we can define a single amplitude, ϵa_b , where a_b is the radius of the semi-cylindrical bubble ($a_b = 40 \mu\text{m}$), which takes into consideration the presence of multiple modes of oscillation. It is also noted here that the surface of the bubble, at the regular operating frequencies [21] is a ‘no-stress’ boundary. The surrounding walls form a ‘no-slip’ boundary. It is seen from previous work that the resultant flow field is 2-D in nature [7,11,12]. The resulting flow field can be expanded in ϵ . The first order expansion results in a strictly periodic component. The second order expansion results in a flow that has a steady part as well as a periodic component. Averaging these components over time results in only the steady flow remaining which we call the steady streaming flow. Over a wide range of frequencies this steady streaming flow is consistently a pattern of two symmetric closed-loop vortices, as shown in Fig. 1.1. These vortices draw fluid towards the bubble and push it upwards along the pole of the bubble.

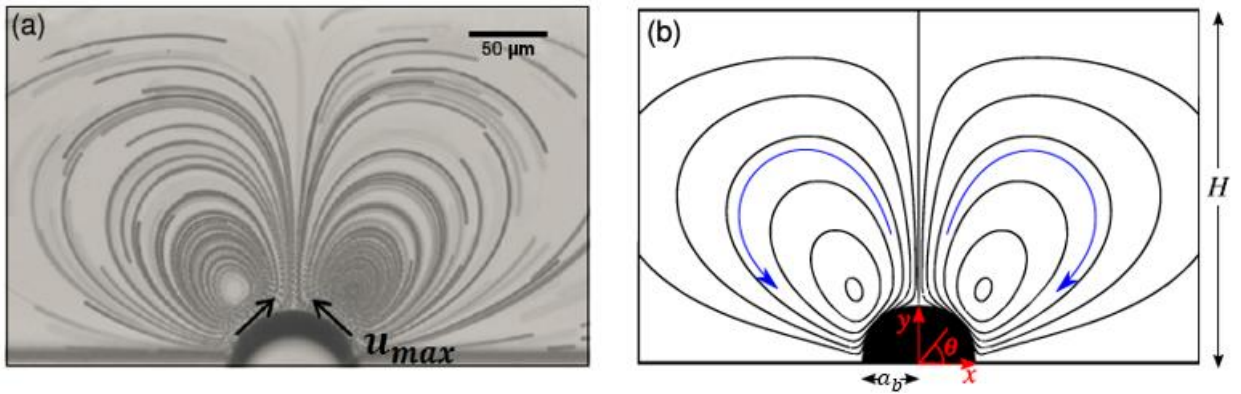


Figure 1. 1: Steady streaming flows generated by bubble oscillations..

1.3 SUPERPOSITION OF POISEUILLE AND STREAMING FLOW

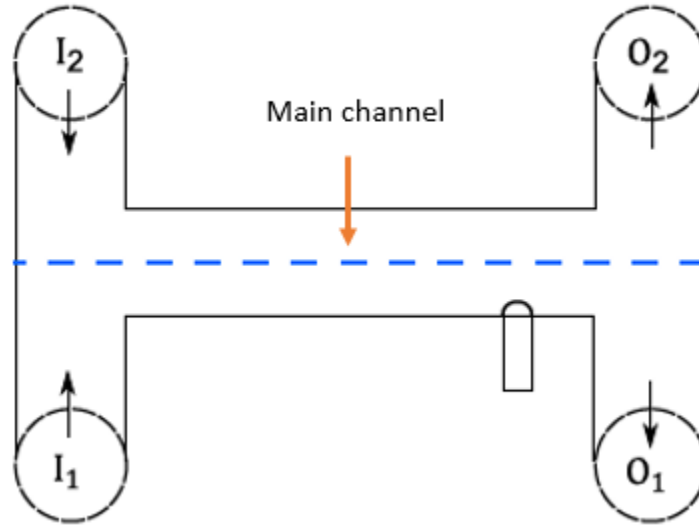


Figure 1. 2: Figure shows the schematic of a typical device. I_1 and I_2 are inlets O_1 and O_2 are outlets

We first describe the experimental parameters and setup used in [5,18,19]. Our experimental setup combines the steady streaming flow with an imposed transport flow through the main channel. The presence of this imposed channel flow greatly alters the overall shape of streamlines near the bubble. Even a relatively slow transport flow forces the vortices to be assymetric by shrinking the upstream vortex and expanding the downstream vortex. Figure 1.3 shows two representative resultant flow field (Poiseuille flow from left to right). By volume conservation of incompressible fluids, we get a number of open streamlines that in the case of slow transport (Figure 1.3 a) go past the surface of the bubble in a narrow bundle. Figure 1.3 b shows a case (more relevant for the current work) with a large transport flow which has eliminated the presence of the upstream vortex. It should be emphasized that we use “streamline” as a short-hand here for a Lagrangian pathline of a liquid particle

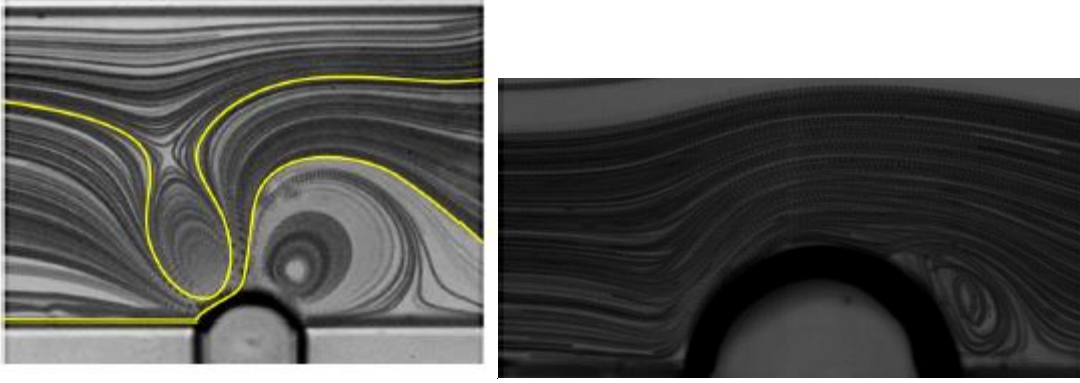


Figure 1. 3: Streamline picture of typical flow in a)previous work b) current work (Note magnification is different, bubbles are of same size) The upstream vortex is absent in the second case

(as would be observed in an experiment as a passive-tracer trajectory), averaged over the short (oscillatory) time scale. This Lagrangian flow field therefore contains the proper Stokes drift terms [2, 13, 14] that distinguish it from the time-averaged Eulerian field. We can expect the overall shape of the flow field to be dictated by the relative strengths of the Poiseuille and streaming flows, as captured by the parameter $s = \bar{u}_p/u_{max}$. Here \bar{u}_p refers to the average velocity of the Poiseuille flow and u_{max} refers to the maximum velocity seen in the streaming flow (Figure 1.1). In Figure 1.3 we see two distinctly different cases of this flow. In the Figure 1.3 a which was characteristic of the previous work there are closed streamline loops upstream and downstream of the bubble. The uppermost point of the upstream loop marks a hyperbolic point with an associated critical streamline. This loop is clearly missing in the Figure 1.3 b which is more characteristic of the experiments in this work. The reasons for this change are explained in later parts of this thesis. Previous publications by this research group have developed a description of the steady component of streaming flow from a semi-cylindrical bubble [7, 10, 11]. Since we are here considering a combination of Poiseuille flow and streaming flow, it is useful to define two kinds of Reynolds numbers (i) $Re_s = u_{max}a_b/\nu$, corresponding to the fast streaming flow near the bubble, and (ii) $Re_p = \bar{u}_p H/\nu$ where ν refers to the viscosity of the

fluid and H is the channel height (seen in Figure 2.2) corresponding to flow gradients over the channel height. We find that the streaming flow at low Reynolds number is a Stoke's flow. Since Re_p is also always smaller than unity, we model the net flow, to leading order in Reynolds number, as a linear superposition of streaming and Poiseuille flow fields. The stream function ψ_s describing the steady streaming flow is given analytically in a half-space ($h \rightarrow \infty$) at any driving frequency by a singularity expansion [7, 10]. Here e_1 and f_1 are constants that can be determined based on certain experimental parameters such as bubble size and frequency. ψ_{osc} is used to express the oscillatory component of the flow. ψ_p expresses the stream function of a Poiseuille flow [15,20]. The net two-dimensional flow satisfying both bubble and wall boundary conditions is given by the superposition.

$$\psi_s = \frac{3}{8r^2} \left(1 + \frac{16}{3} e_1 r \sin \theta + \frac{8}{3} f_1 \sin^2 \theta \right) \sin 2\theta + O(r^{-3}) \quad (1.1)$$

$$\psi = \psi_{osc} + \epsilon(\psi_s + s\psi_p) \quad (1.2)$$

Once we have the stream function ψ it is easy to derive the corresponding velocities of interest from it. We will use this stream function later to determine the velocity fields for simulation in Section 3.3

1.4 PARTICLE BEHAVIOR AND MEASUREMENT OF FORCES

In the previous work [18,19] it was observed that there are size dependent forces on particles by observing quantitative differences in particle trajectories. This can be seen in Figure 1.4. where we can see different behavior between particles of two different sizes. Particles of two different radii (2.5 μm , 5 μm) enter the flow in the lower half of the main channel. Particles of radius 5 μm ($a_p = 5 \mu\text{m}$) can be seen to be redirected to the upper channel T junction by this

flow. Whereas particles of radius $2.5\text{ }\mu\text{m}$ ($a_p = 2.5\text{ }\mu\text{m}$) are redirected to the lower T junction channel. This shows us that the particles of larger radius see more repulsion in comparison to its smaller counterpart.

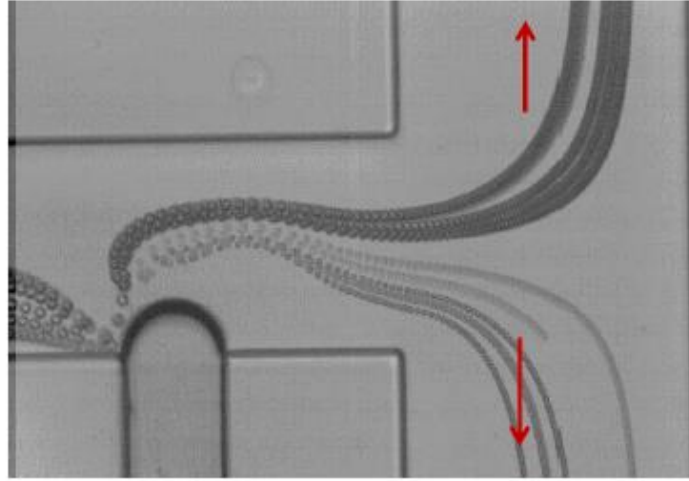


Figure 1. 4: Figure showing sorting behavior because of different forces felt by different particles

The previous publication also develops a method of measuring the force on a particle. Particles of smaller size ($a_p = 0.5\text{ }\mu\text{m}$) are used as proxies for streamlines. It is seen that when a larger particle is close to the bubble surface it crosses several streamlines outward. This is seen in Figure 1.5.

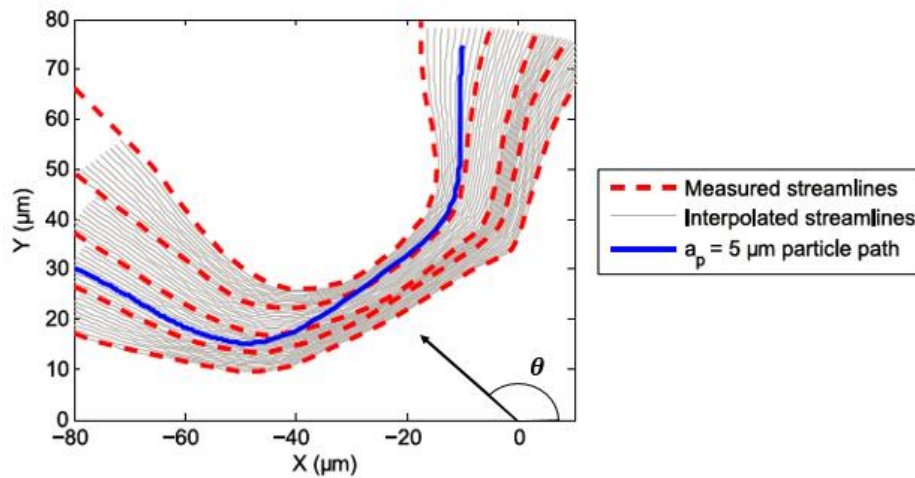


Figure 1. 5: large particle crossing streamlines with 'repulsive forces'

The larger particle follows a trajectory that intersects with many of our interpolated streamlines. At any of these points of intersection, the large particle speed \mathbf{v}_p can be decomposed into components that are respectively parallel and perpendicular to the streamline that is crossed, we call these $v_{||}$ and v_{\perp} . v_{\perp} is the direct measure of the action of lift in these experiments. If we assume that this velocity represents overdamped motion by Stokes drag, we obtain an estimate for the lift force acting on the particle as

$$F_l = 6\pi\mu a_p v_{\perp} \quad (1.3)$$

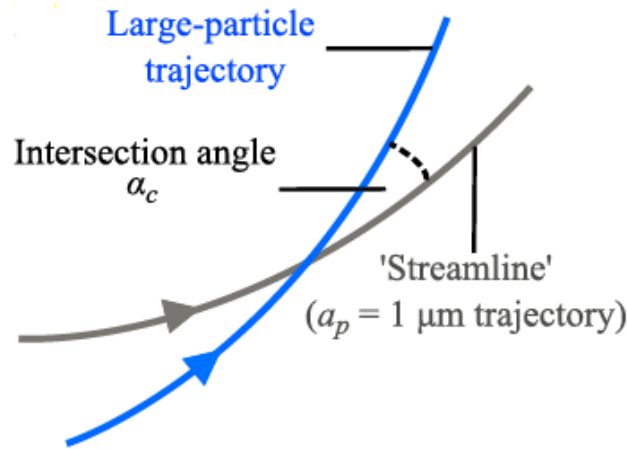


Figure 1. 6: Shows the measuring of the angle between streamlines and particle trajectories

To get a measure of the value of v_{\perp} we just measure particle velocity and the intersection angle α_c (as depicted in Figure 1.6). Then we can use the projection of the velocity so that the Force on the particle is

$$F_l = 6\pi\mu a_p |\mathbf{v}_p| \sin(\alpha_c)$$

1.5 INSTANTANEOUS VS NET DISPLACEMENT

The result shown in Figure 1.7 shows the instantaneous force of a particle as it moves across the bubble.

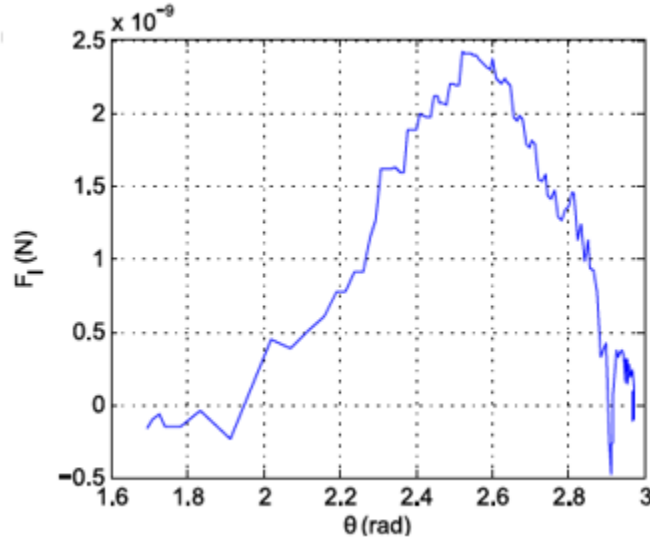


Figure 1. 7: The variation of Force as the particle goes past the bubble surface

It is seen here that a majority of particle and bubble interaction occurs in a small portion of the trajectory. Thus, a high magnification was used to capture detailed data about this portion of the trajectory. This is however not the only interesting case especially for the experiments that we will conduct. The experiments that are of interest in this work are those with high values of s as seen in Figure 1.3 b where interaction between the bubble and the particle is significant over a larger portion of the trajectory. Since we are interested in a large portion of the trajectory we cannot use high magnification to capture our data. Additionally, since the streaming is weak the forces on the particle are also weaker. This weaker force results in smaller values of the angle α_c . For these reason, the above method is not suitable to analyze these cases since the data captured would have too much noise in order to calculate small differences in angles accurately. In these cases, we are more interested in the net effect of the journey of the particle past the bubble rather than the instantaneous forces on the particle. Thus, the quantity that would really interest us is

$\int_{t=0}^{\infty} v_{\perp}$. Since we are looking for the net effect rather than instantaneous forces we opt to use a different methodology which is discussed in Section 4.3.

CHAPTER 2: EXPERIMENTAL SETUP

2.1 SETUP DETAILS

The microfluidic devices are manufactured from polydimethylsiloxane (PDMS) using techniques similar to those described in previous works by this research group [3, 4, 7]. Standard photolithography procedures are used to create 100 μm tall SU-8 molds on silicon wafers. PDMS mixture (90% w/w resin, 10% w/w hardener) is poured onto the SU-8 molds and is allowed to harden for 24 hours. These device layers are then peeled from the molds and bonded to a flat PDMS layer using an oxygen plasma treatment. Inlets and outlets are connected using 1/32 in. tubing. A schematic of a typical device design is shown in Figure. 2.1. The channel depth $D=100\ \mu\text{m}$ is dictated by the height of the SU-8 layer. Inlet channels lead into a main channel perpendicular to which a blind side channel of width $w=80\ \mu\text{m}$ is placed. When aqueous solution enters the main channel, the PDMS's hydrophobicity ensures that air is trapped in the side channel, forming a semi-cylindrical bubble. The device is bonded to a glass slide to which a piezoelectric transducer (Physik Instrumente, Germany) is then attached.

A function generator (model 7075, Hioki) and an amplifier (model 7500, Krohn-Hite, set to 100x amplification) provide sinusoidal signals to the piezotransducer which then ultrasonically excite the bubble. Bubble size can vary due to temperature changes and consequent diffusive transport of gas, but is maintained by modulating the external temperature through evaporative cooling or environmental heating.

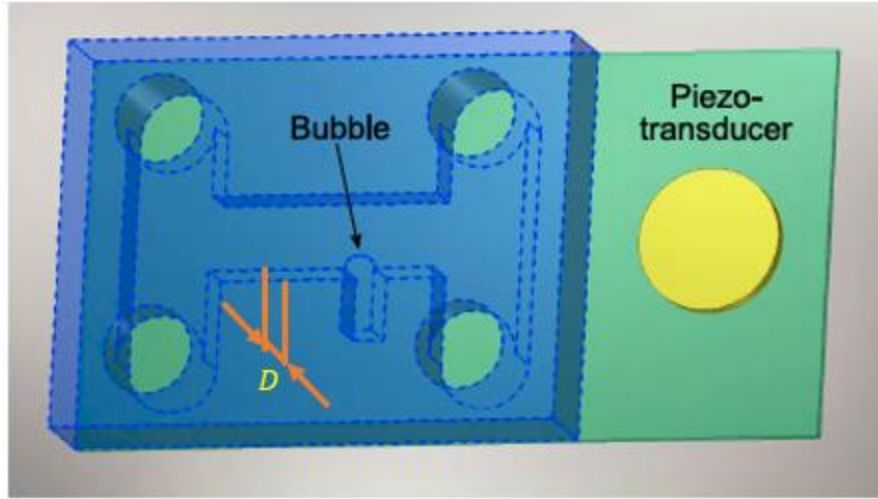


Figure 2.1: Illustration of typical device design indicating inlets/outlets, the position of the bubble and the piezoelectric transducer

Particle solutions consist of 2 μm , 5 μm , 10 μm and 20 μm diameter microparticles made from either Polystyrene (PS) latex or Polymethyl Methacrylate (PMMA) (Magsphere and Phosphorex) suspended in fluid (between 0.0025 % to 0.01 % by volume). Some experiments may include just pure water, others use glycerol/water solution (23% glycerol w/w made to match the density of the Polystyrene) and the density of the solution can be increased as necessary by the addition of Sodium Polytungstate. Sodium Polytungstate is used to increase the fluid density to bring it close to that of PMMA without having any major effect on fluid viscosity (ρ_f). We will refer to the size of particles below in terms of their radius a_p . 1% w/w Tween 20 surfactant was added in order to prevent particle agglomeration. We use syringe pumps (PHD Ultra, Harvard Apparatus and EW-74905, Cole-Parmer) to infuse constant fluid flow rates through each inlet channel. A high-speed camera (Phantom v310, Vision Research) is used to capture videos through an inverted microscope (IX71, Olympus). In all experiments in this work the videos are stroboscopic (ie the framerate of the video matches the oscillation frequency). We use Mtrack2, a plugin for the image processing program ImageJ, to record particle trajectories. Further processing of the trajectories is done using MATLAB code.

2.2 DEVICE AND EXPERIMENTAL SETUP

Section 2.1 provided a broad overview of the general design and manufacture of our microfluidic devices. We now focus on the specifics of the devices used for characterizing the density dependent behavior of different particles.

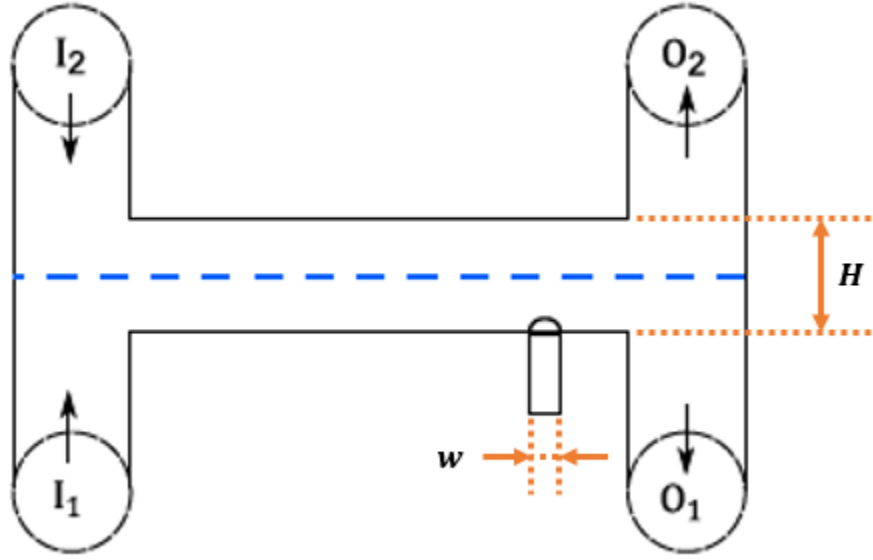


Figure 2. 2: Schematic of device inlets and outlets. Particle solution is infused through I_1 while glycerol-water solution without particles enters through I_2 . The outlets O_1 and O_2 are left open to the atmosphere. The dashed blue line represents the stagnation streamline dividing the upper and lower halves of the flow and is parallel to the flow direction in the absence of an applied driving.

A schematic of a typical device design is shown in Figure 2.2. Two inlet channels lead into a main channel which then bifurcates into two outlet channels. Main channel heights of $H = 250\mu m$ is used and the channel depth is $D = 100\mu m$. The blind side channel of width $w = 80\mu m$ is placed perpendicular to the main channel and holds the semi-cylindrical microbubble. As previously described, our experimental setup combines the steady streaming flow with an imposed Poiseuille flow. In the two inlet / two outlet design we have described above, when the piezo transducer is turned off, the flow is laminar and symmetric with a stagnation streamline evenly dividing the bottom and top halves of the flow, as indicated in Figure. 2.2. The fluids entering inlets I_1 and I_2 exit through outlets O_1 and O_2 , respectively. While this remains the case

when the streaming flow is turned on, the shapes of the streamlines are altered as previously shown in Figure 1.3.

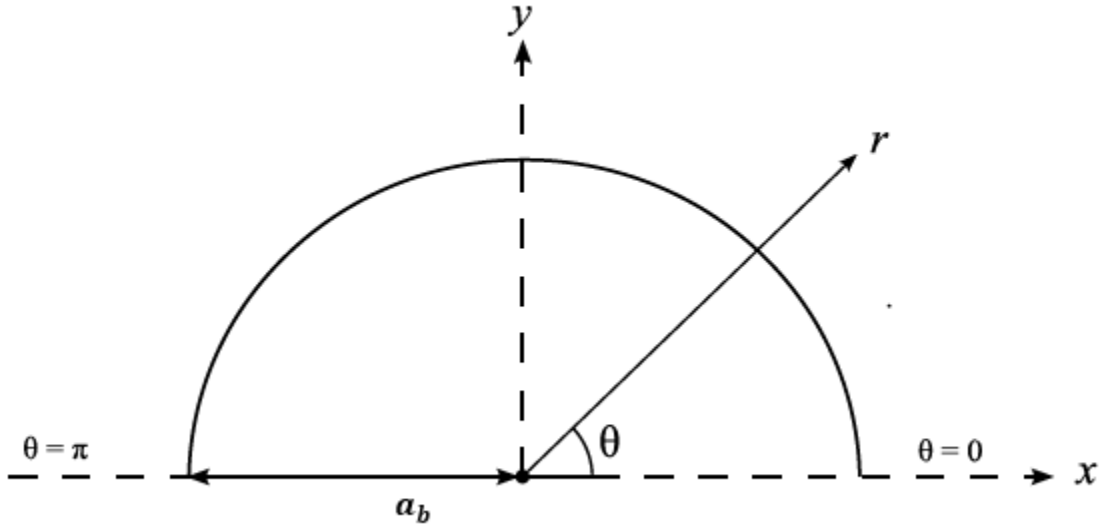


Figure 2.3: Definition of coordinates.

2.3 DEFINITION OF COORDINATES

The coordinates we will use to describe the bubble and flow geometry are defined in Figure. 2.3. Since the flow is two dimensional any point in the flow field can be defined by its distance r from the center of the bubble and its angular position θ . The channel walls are present at $y = 0$ and $y = H$. The bubble is centered at the point $x = 0$ and it is pinned to the walls at the points $x = \pm a_b$.

a_b represents the radius of the pinned bubble. In theoretical descriptions, the bubble surface is then given by $r = r_b(\theta, t)$ with an average position $\langle r_b \rangle = a_b$. However, this is not necessarily true in experiment, where the bubble is generally not perfectly semi-cylindrical.

2.4 FLOW WITH WEAK STREAMING

When s is small (strong streaming) particles are forced close to the surface of the bubble because streamlines in such a flow form a narrow bundle near the bubble surface (refer Section 1.3). In this work, we are interested in studying a wider range of behavior seen by the particle due the nature of the variation in forces that it experiences, particularly in cases of density mismatch as well as in cases where there is a larger distance between the particle and the bubble when compared to previous work [5,18]. It will also be seen in the following chapter (Section 3.3) that there is a rich variation in the nature of forces and how they vary with density mismatch as well as distance from the bubble. In order to study these variations, we need to have flows which have the capacity to vary the distance of approach between the bubble and the particle. Due to this reason, the experiments conducted in this work make use of a weaker streaming (larger value of s) as mentioned previously in Section 1.5. As seen in Figure 1.3 b the streamlines in such flows allow for large variation in the distance of closest approach between the bubble surface and the particle. Thus, by running experiments with weak streaming we obtain a new experimental parameter and can study a larger variation of particle trajectories and consequently their behavior as they pass the bubble.

CHAPTER 3: THEORY

Note: The theory discussed in this chapter was largely developed by Bhargav Rallabandi and Siddhansh Agarwal. This author's chief contribution was to collect experimental data that could then be compared to theoretical results.

3.1 MAXEY-RILEY EQUATION

We have already seen an introduction to the 2-D superposition of streaming flow and Poiseuille flow in Section 1.3. Now we look at the theoretical model that can be used to predict the motion of a particle which is suspended in this flow. To do so we start with the Maxey Riley equation [16] which describes the motion of an inertial spherical particle of density ρ_p in an ambient flow field (\mathbf{u}). The velocity of the particle at position \mathbf{r}_p is denoted by \mathbf{v}_p . Because we are dealing with particles which potentially get very close to an interface and experience strong displacements (as seen in Section 1.4) we need a theory that can model these forces. This is provided quite nicely by lubrication force approximations as seen in which is responsible for the penultimate line in equation 3.1. Note that we have added an extra exponential decay to the lubrication term because it is only effective for surface to surface distances between particle and interface shorter than the boundary layer thickness [19,22]. We also add the inviscid correction factor (last term in the last line of equation 3.1) to this equation as given in [22]. Note that this term is unconditionally attractive. After non dimensionalizing, using a velocity scale $U_0 = \epsilon a_b \omega$, timescale $t_0 = a_b / U_0$ and $Re_p = a_p^2 / \nu t_0$ and rearranging the equation we get

$$\begin{aligned}
\left(\frac{\rho_p}{\rho_f} + \frac{1}{2}\right) \frac{d\mathbf{v}_p}{dt} &= \frac{3}{2} \frac{D\mathbf{u}}{Dt} - \frac{9}{2} Re_p^{-1} \left(\mathbf{v}_p - \mathbf{u} - \frac{1}{6} \frac{a_p^2}{a_b^2} \nabla^2 \mathbf{u} \right) \\
&\quad - \frac{9}{2} \pi^{-\frac{1}{2}} Re_p^{-\frac{1}{2}} \int_{-\infty}^t \frac{\frac{d}{d\tau} \left[\mathbf{v}_p(\tau) - \mathbf{u}(\mathbf{r}_p(\tau), \tau) - \frac{1}{6} \frac{a_p^2}{a_b^2} \nabla^2 \mathbf{u}(\mathbf{r}_p(\tau), \tau) \right]}{\sqrt{t - \tau}} d\tau \\
&\quad - \frac{9}{8} Re_p^{-1} \frac{a_p}{a_b} \left(\frac{\hat{\mathbf{n}}_b \cdot (\mathbf{v}_p - \mathbf{u}_b) e^{-\frac{\mathbf{r}_p - \mathbf{r}_b}{\delta}}}{\hat{\mathbf{n}}_b \cdot (\mathbf{r}_p - \mathbf{r}_b) - \frac{a_p}{a_b}} \right) \hat{\mathbf{n}}_b + \frac{1}{4} a_p^2 \nabla \mathbf{u} : \nabla (\nabla \mathbf{u})
\end{aligned} \tag{3.1}$$

where \mathbf{u}_b and \mathbf{r}_b is the velocity and position of the point on the interface that is closest to the particle. The effective boundary layer thickness is given by δ . The operators d/dt and D/Dt denote time derivatives following particle and fluid motion.

$$\frac{d\mathbf{u}}{dt} = \frac{\partial \mathbf{u}}{\partial t} + \mathbf{v}_p \cdot \nabla \mathbf{u} \tag{3.2}$$

$$\frac{D\mathbf{u}}{Dt} = \frac{\partial \mathbf{u}}{\partial t} + \mathbf{u} \cdot \nabla \mathbf{u} \tag{3.3}$$

We can simplify the Maxey Riley equation by neglecting the Faxen terms (term including the Laplacian of velocity) since $\frac{a_p}{a_b} \ll 1$ and the Basset history term (terms including the integral) since they have a very small effect on the effective particle trajectory [17].

For compactness, we introduce

$$h(x_p) = \hat{\mathbf{n}}_b \cdot (\mathbf{r}_p - \mathbf{r}_b) - \frac{a_p}{a_b} \tag{3.4}$$

$$\gamma = \frac{a_p}{4a_b} \tag{3.5}$$

$$\hat{\mu} = \left(\frac{\rho_p}{\rho_f} + \frac{1}{2} \right) \cdot \frac{2}{3} \tag{3.6}$$

$$\lambda = a_p^2 \omega / 3\nu \quad (3.7)$$

The term $\hat{\mu}$ is a measure of the density mismatch between the particle and the fluid. It is 1 for a density matched case. Due to the choice of length and time scales for the non dimensionalization, the particle's velocity $\mathbf{v}(\tau)$ is related to its position $\mathbf{r}(\tau)$ as

$$\frac{d\mathbf{r}_p}{d\tau} = \epsilon \mathbf{v}_p \quad (3.8)$$

We now rescale time by the oscillatory time scale introducing $\tau = t/\epsilon$. After making all the above changes the equation 3.1 becomes

$$\begin{aligned} \lambda \hat{\mu} \frac{d^2 \mathbf{r}_p}{d\tau^2} + \left(1 + e^{-\frac{h(\mathbf{r}_p)}{\delta}} \gamma \frac{\hat{\mathbf{n}}_b}{h(\mathbf{r}_p)} \hat{\mathbf{n}}_b \right) \frac{d\mathbf{r}_p}{d\tau} \\ - \epsilon \left\{ \lambda \left(\frac{\partial \mathbf{u}}{\partial \tau} + \mathbf{u} \cdot \nabla \mathbf{u} \right)_r + \frac{32}{9} \epsilon \lambda \gamma^2 \nabla \mathbf{u} : \nabla (\nabla \mathbf{u}) + \mathbf{u}|_r \right. \\ \left. + e^{-\frac{h(\mathbf{r}_p)}{\delta}} \gamma \frac{\hat{\mathbf{n}}_b \cdot \mathbf{u}_b}{h(\mathbf{r}_p)} \hat{\mathbf{n}}_b \right\} = 0 \end{aligned} \quad (3.9)$$

We note that the particle Reynolds number $Re_p = \frac{\epsilon a_p^2 \omega}{\nu}$, $\lambda \epsilon, \gamma \ll 1$. This is important since we need these parameters to be small so that equation 3.9 is valid.

3.2 SLOW TIME SOLUTION TO PURELY RADIAL CASE

In the flows that we study in experiments (described in Section 1.3 and 2.4) we see that the transport across the bubble is primarily azimuthal while the forces act primarily in the radial direction. This is not necessarily true throughout the journey of the particle but during the time when the particle is close to the bubble this approximation proves useful in helping to determine the asymptotic behavior of particles. This allows us to make a 1-D simplification to the Maxey Riley equation where we are only looking at the radial variation. We define the distance between

the surface of the bubble and the surface of the particle as $X = r_p - 1 - 4\gamma$. This changes the equation 3.9 as follows. Here scalar quantity u is the radial component of the velocity vector \mathbf{u} . In this 1-D radial approximation the bubble radius motion is described by \mathbf{r}_b is $1 + \epsilon\Delta R(\tau)$ [46, 22]

$$\begin{aligned} \lambda\hat{\mu}\frac{d^2X}{d\tau^2} + \left(1 + \frac{e^{-\frac{X}{\delta}}\gamma}{X - \epsilon\Delta R}\right)\frac{dX}{d\tau} \\ - \epsilon\left\{\lambda\frac{\partial u}{\partial\tau}\Big|_X + \frac{32}{9}\epsilon\lambda\gamma^2\nabla\mathbf{u}:\nabla(\nabla\mathbf{u}) + u|_X + \frac{e^{-\frac{X}{\delta}}\gamma}{X - \epsilon\Delta R} + \epsilon\lambda\left(u\frac{\partial u}{\partial r}\right)_X\right\} \\ = 0 \end{aligned} \quad (3.10)$$

We now invoke a time scale separation to the problem by introducing a new ‘slow time’ scale to the problem $T = \epsilon^2\tau$ and thus transform $X(\tau) \rightarrow X(\tau, T)$. We then seek a solution of the form $X(\tau, T) = X_0(\tau, T) + \epsilon X_1(\tau, T) + \epsilon^2 X_2(\tau, T) + \dots$. We now attempt to apply perturbation theory to this equation for streaming flows with the ambient flow field $u = u_{osc} + \epsilon U_L$. Here u refers to the oscillatory component which oscillates as $u_{osc} = Ue^{i\tau}$ and U_L refers to the Lagrangian background flow. We attempt to make an expand these equation to $O(\epsilon^2)$. The $O(1)$ solution turns out to simply be $X_0(\tau, T) = X_0(T)$. The $O(\epsilon^2)$ equation for this problem allows us to get a first order ODE for $X_0(T)$ which is of the form

$$\begin{aligned}
\frac{dX_0}{dT} = & \frac{\lambda X_0}{X_0 + e^{-\frac{X_0}{\delta} \gamma}} \left[-\frac{e^{-\frac{X_0}{\delta} \gamma} (1 - U_0) U_0'}{2} \frac{X_0 (\hat{\mu} + 1) + e^{-\frac{X_0}{\delta} \gamma}}{\left(X_0 + e^{-\frac{X_0}{\delta} \gamma} \right)^2 + X_0^2 \hat{\mu}^2 \lambda^2} \right. \\
& + (\hat{\mu} - 1) \frac{U_0 U_0'}{2} X_0 \frac{X_0 (\lambda^2 \hat{\mu} - 1) - e^{-\frac{X_0}{\delta} \gamma}}{\left(X_0 + e^{-\frac{X_0}{\delta} \gamma} \right)^2 + X_0^2 \hat{\mu}^2 \lambda^2} \\
& \left. + \frac{16}{9} \gamma^2 \left(\frac{2U_0}{X_0^2} \left(U_0' - \frac{U_0}{X_0} \right) + U_0' U_0'' \right) \right] + \frac{X_0 U_L}{X_0 + e^{-\frac{X_0}{\delta} \gamma}}
\end{aligned} \tag{3.11}$$

The last term involving U_L describes the passive transport that the particle would undergo. It is seen that on integration this term itself has no net effect of the net displacement of the particle.

Note the prefactor of $\frac{X_0}{X_0 + e^{-\frac{X_0}{\delta} \gamma}}$ is essentially a geometric exclusion term that prevents the particle from penetrating the surface of the bubble. This prefactor becomes close to 1 for large values of X_0 and only significantly affects the behavior at small X_0 . The presence of the first three terms on the RHS indicate net deviation from this. The first of these terms is independent of $\hat{\mu}$ and is always positive (for the physical case of a flow field with $U_0' < 0$) indicating that it always causes the particle to be further repelled from the bubble surface in comparison to a fluid element. However, the second term can be both positive or negative based on the values of $\hat{\mu}$ and λ . The third term is a purely negative term (again for physically relevant flow fields). The combination of these terms if negative in principle can allow the particle to be attracted to bubble surface in comparison to a fluid element.

In order to gain insight into the parameter dependence of this ODE, we focus on a representative case with a semi-cylindrical bubble. Because of this we let the oscillatory component of the

velocity to decay as $U_0(r) = 1/r$. To study the variation of equation 3.11 with the parameters $\hat{\mu}$ and λ we run simulations with $U_L = 0$. In the process of solving these equations we make a change of variables. We report the results in terms of $\hat{\kappa} = \hat{\mu} - 1$, γ and δ . The substitutions to transform equation 3.11 to an easier form are given in equation 3.12 and 3.13. We note here that now $\hat{\kappa}$ describes the density mismatch while γ describes particle size.

$$\hat{\mu} = \hat{\kappa} + 1 \quad (3.12)$$

$$\lambda = \frac{32\gamma^2}{3\delta^2} \quad (3.13)$$

We generate two different phase plots depending on which region we find ourselves in. First, we acknowledge that this is a 1-D model. In setting the $U_L = 0$ there are only two possible behaviors for the suspended particle. In the repulsive case, the particle is repelled indefinitely from the bubble surface. In the attractive case, there exists an equilibrium point ($\frac{dX_0}{dt} = 0$ in equation 3.11, see [22]). After running the simulation with different experimentally viable values of $\hat{\kappa}$ and γ at a constant value of δ ($\delta \in \{0.095, 0.130\}$ two different viscosities for water and 24% water-glycerol mixture) we can determine which of the parameters lead to which of the two cases. We present the results of these runs in Figure 3.1 and 3.2. The parameter values for the experiments which are discussed in Chapter 4 are indicated on the Figure 3.1. This figure describes the ‘attractive’ behavior. The measure of the attractive behavior is given as the distance of the equilibrium point from the bubble surface (given by h_s). The smaller the distance the stronger the attraction. We see that there is one contiguous region where attraction is possible. It is also clear that this attraction is stronger when we have either larger denser particles or smaller lighter particles.

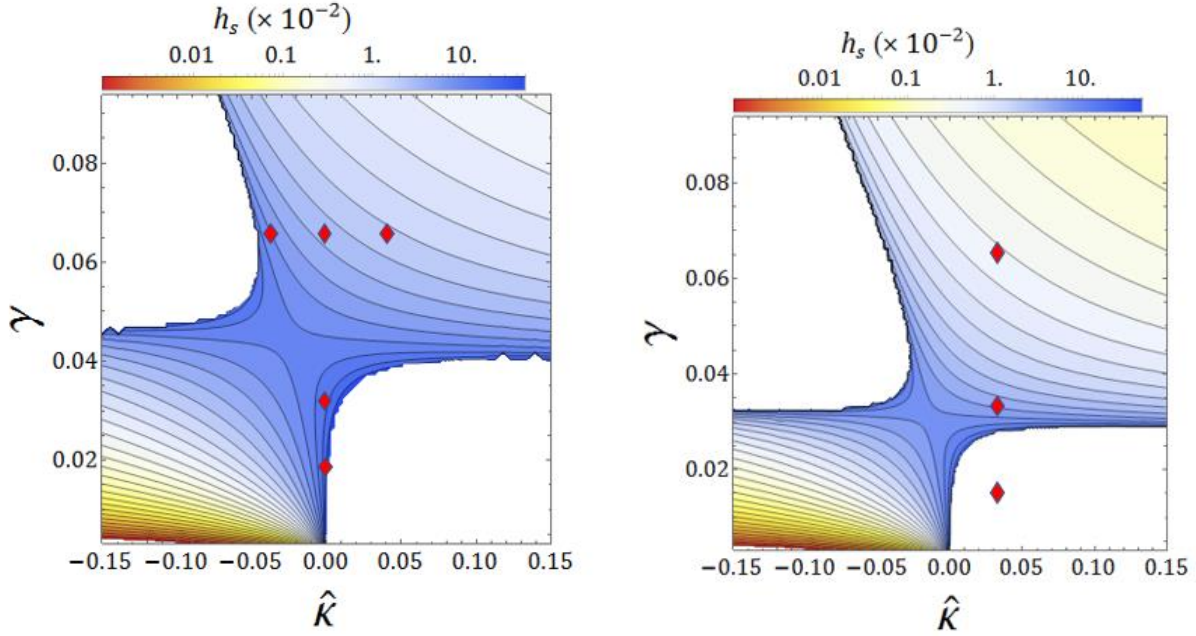


Figure 3. 1: Plot showing particle behavior for different values of \hat{K} and γ in attractive regime for values of a) $\delta = 0.130$ (for glycerol water solution) b) $\delta = 0.095$ (for pure water). Red diamonds indicate the parameter combinations used in the experiments of Chapter 4

The latter is not experimentally viable because small particles experience forces of very small magnitude thus making it difficult to distinguish and measure these effects. The former (consisting of larger heavier particles) shows much more promise in experiments. For the plot dealing with repulsion we measure the time taken for a particle to be repelled by 1 particle diameter (8γ) from a fixed initial condition (denoted by T_{2ap}). The smaller this time the stronger the repulsion. The Figure 3.2 shows these results. We see two distinct regions of repulsion here (for smaller heavier particles and for larger lighter particles). It is interesting to note that these regions are both accessible via experiments although experiments have only been conducted in one of these due to practical experimental constraints.

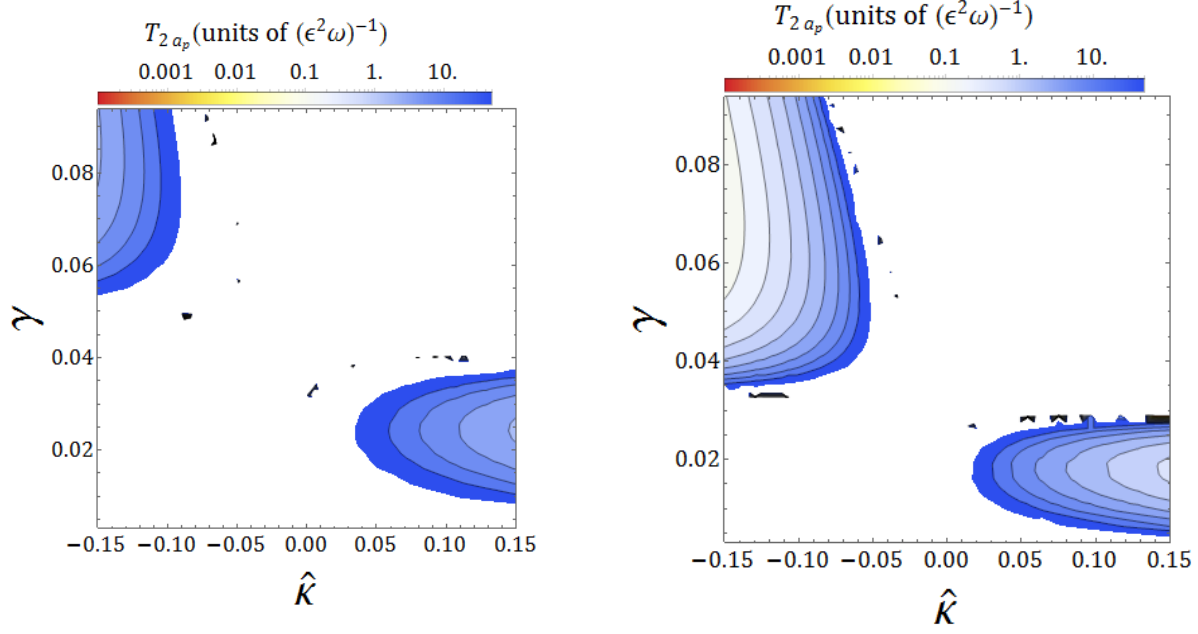


Figure 3. 2 Plot showing particle behavior for different values of \hat{K} and γ in repulsive regime for values of a) $\delta = 0.130$ b) $\delta = 0.095$

There are however certain problems with directly translating this theory to experiments. Firstly the Lagrangian flow field (U_L) seen in experiments is 2-D which resists a simple 1-D theoretical model. It has been stated before that we have used the 1-D assumption, i.e., that over a large range of the trajectory the forces are in a purely radial direction whereas transport is purely azimuthal. We have stated previously in Section 2.4 that the current experiments use flows that have much weaker streaming. Weaker streaming translates into forces of smaller magnitude on particles and thus the above assumption of radial forces being able to completely explain deviations in particle trajectories fails. We see that the phase diagram above (Figure 3.1 and Figure 3.2) only gives us an asymptotic estimate of the behavior of a particle in a purely radial case when they can be tracked for arbitrarily long periods of time. However, any particle following a trajectory past the bubble surface has a finite amount of time where it is close to the interface. During this period, a particle will move towards its equilibrium point or be repelled (depending on which region of the phase plot it falls in). Hence even particles which are density

matched ($\hat{\kappa} = 0$), which are completely in the attractive regime according to Figure 3.1, will be repelled if they have an approach distance which is closer to the bubble surface than the equilibrium distance. Even though we have stated that this version of the theory does not offer quantitative predictions there are instances where the asymptotic predictions of this model are very useful. A version of this equation is used to great effect in the previous work [19]. A version of this theory has also been used for a spherical bubble has been used to successfully model particle trapping [22,23]. This set of equations can be used to predict a region of the parameter space where we expect to see attraction. It is also seen later in Section 4.5 that the predictions made by this model about the range of attractive and repulsive regions are consistent with all the experimental results. However, since the previous equation does not quantitatively predict the particle behavior in experiments that follow it motivates a 2-D version of the above theory.

3.3 SLOW TIME SOLUTION FOR 2-D STREAMING FLOWS

Modeling this system in 2-D is done in a very similar way as the 1-D modelling. We start from equation 3.14 which is a simplified version of equation 3.9. There are two simplifications we make to the equation 3.9 to simplify the process of finding a solution. The first simplification is the absence of the inviscid correction term [22]. The second is that the lubrication term does not have an exponential decay attached to it. It is seen in practice that the slow time solution for particle position that is obtained after making these simplifications is still fairly accurate. We describe later in this section how the inclusion of these effects could potentially help refine the theoretical predictions. In this case the flow field that we use to describe the background flow is that which is discussed toward the end of Section 1.3. since we can obtain a form of the stream function $\psi = \psi_{osc} + \epsilon(\psi_s + s\psi_p)$ we can obtain the 2-D velocity fields with the cartesian components u_{osc}, v_{osc} and u_L, v_L from these stream functions.

$$\lambda \hat{\mu} \frac{d^2 \mathbf{r}_p}{d\tau^2} + \left(1 + \gamma \frac{\hat{\mathbf{n}}_b}{h(\mathbf{r}_p)} \hat{\mathbf{n}}_b \right) \frac{d\mathbf{r}_p}{d\tau} - \epsilon \left\{ \lambda \left(\frac{\partial \mathbf{u}}{\partial \tau} + \mathbf{u} \cdot \nabla \mathbf{u} \right)_r + \mathbf{u}|_r + \gamma \frac{\hat{\mathbf{n}}_b \cdot \mathbf{u}_b}{h(\mathbf{r}_p)} \hat{\mathbf{n}}_b \right\} = 0 \quad (3.14)$$

We then do the same type of time scale separation in cartesian co-ordinates as above to find some solution of the particle trajectory. An intermediate result of solving the first order equation of the time scale separation we get solutions for the first order of particle position of the form 3.15 and 3.16 (Note that A_1, A_2, B_1, B_2 are dependent on initial conditions).

$$x_1(\tau, T) = \int (u_{osc} + s_{osc}) d\tau + A_1(T)(1 - e^{-k_1 \tau}) + B_1(T) \quad (3.15)$$

$$y_1(\tau, T) = \int (v_{osc} + t_{osc}) d\tau + A_2(T)(1 - e^{-k_2 \tau}) + B_2(T) \quad (3.16)$$

(s_{osc} and t_{osc} are explicitly known functions of the given velocity fields). If we then solve the second order of the time scale separation for particle position in polar co-ordinates we get the equations 3.17 and 3.18.

$$\begin{aligned} \frac{X_0 + \gamma \frac{dr_0}{dT}}{X_0} = & \langle (\int s_{osc} d\tau) \frac{\partial}{\partial r} \left(\lambda \frac{\partial u_{osc}}{\partial \tau} + u_{osc} \right) + (\int t_{osc} d\tau) \frac{\partial}{\partial \theta} \left(\lambda \frac{\partial u_{osc}}{\partial \tau} + u_{osc} \right) \\ & + u_L \cos \theta + v_L \sin \theta \rangle_{X_0} \end{aligned} \quad (3.17)$$

$$\begin{aligned} r_0 \frac{d\theta_0}{dT} = & \langle (\int s_{osc} d\tau) \frac{\partial}{\partial r} \left(\lambda \frac{\partial v_{osc}}{\partial \tau} + v_{osc} \right) + (\int t_{osc} d\tau) \frac{\partial}{\partial \theta} \left(\lambda \frac{\partial v_{osc}}{\partial \tau} + v_{osc} \right) \\ & + v_L \cos \theta - u_L \sin \theta \rangle_{X_0} \\ & + \frac{\gamma X_0}{r_0} \langle (\int (s_{osc} + u_{osc}) d\tau) (t_{osc} + v_{osc}) \\ & - \Delta R (\sin \theta (\int (s_{osc} + u_{osc}) d\tau) - \cos \theta (\int (t_{osc} + v_{osc}) d\tau)) \rangle_{X_0} \end{aligned} \quad (3.18)$$

This is a 2-D version of equation 3.11 whose solution gives us the trajectory of the particle as a function of the slow time. It is not as easy in the 2D case to explicitly separate terms that result in attractive or repulsive particle behavior. However, a numerical solution of this system of first-order ODEs is still relatively straightforward and one can obtain numerical solutions for the particle trajectory. A result of this simulation is shown in Figure 3.3. As is clearly seen this

theory potentially gives us a manner by which we can make theoretical predictions about particle behavior as not only a function of $\hat{\kappa}$ and γ but also as a function of properties of particle trajectory, such as initial condition or closest approach distance to the bubble interface.

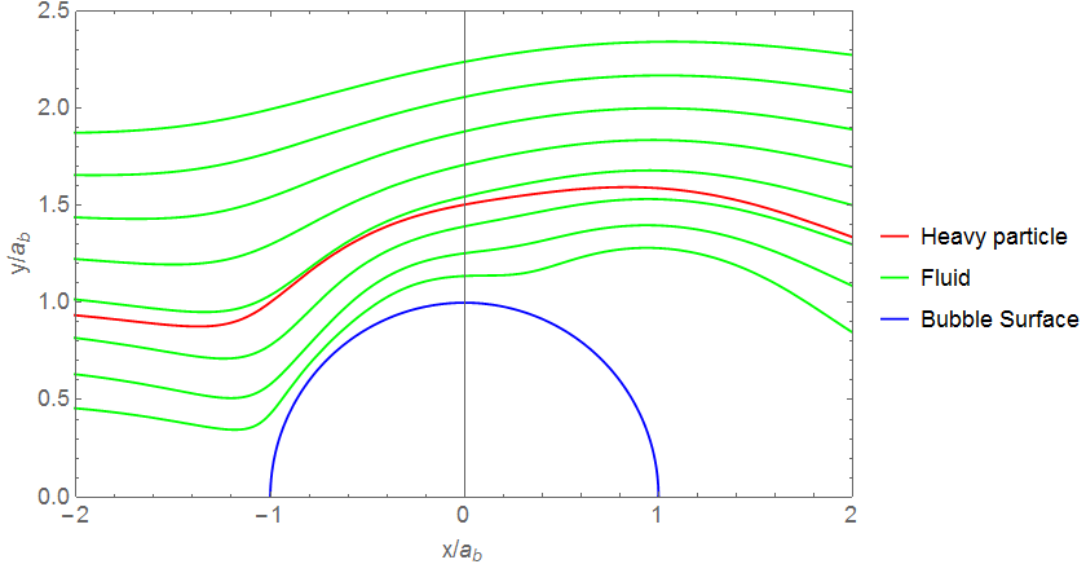


Figure 3. 3: predictions of 2D simulation for $s = 2$, $\gamma = 0.0625$ $\hat{\kappa} = 0.046$ $\delta = 0.130$ and $h_{min} \sim 9.4 \mu m$

We have stated in the beginning of this section that certain simplifications were made to equation 3.9, namely ignoring the exponential decay of the lubrication term and inviscid correction term, that were present in the 1-D version of the slow time theory but not in the above version of the 2-D theory. A further refinement of this 2D theory is possible, considering the effects analogous to the exponential decay of the lubrication force and the inviscid correction in the 1D theory.

However, at present these effects have only been incorporated into the analog of the Maxey-Riley equation (equation 3.9), while explicit slow-time equations analogous to equations 3.17 and 3.18 are not yet available. Nevertheless, numerical solutions on the oscillatory time scale taking these effects into account are obtainable, and can be numerically time-averaged to yield a refined approximation to the slow-time particle path. Future work may also include an instantaneous approximation to the Basset-Boussinesq history term [22, eq 11] in the Maxey-

Riley equation for the specific case of a translating oscillating sphere. However, this untested approximation is not included in the present work.

CHAPTER 4: EXPERIMENTAL RESULTS

4.1 EXPERIMENT SET

Since the goal of the experiments is to obtain experimental evidence of an attractive resultant force on the particle in the streaming flow, experiments are performed in the attractive regime as proposed by the Theory in Section 3.2. To show that these interesting behaviors are influenced by density mismatch we also conduct density matched experiments as a control.

Theory informs us that attractive forces become apparent in combination for simultaneously higher or lower values of the parameters γ and $\hat{\kappa}$ (refer to Figure 3.1). This means that experiments use particles that are denser than the fluid in which they are suspended ($\hat{\kappa} > 0$).

There are some practical limitations which restrict the values of the parameters γ and $\hat{\kappa}$. There is a limit to how far one can vary $\hat{\kappa}$ since buoyant forces will make it extremely difficult to force particles into the device without having them settle. For this reason, the values of we restrict $\hat{\kappa}$ to values between -0.05 and 0.06 (Note that these limits are for the largest particle size, smaller particles allow for more extreme values). The parameter γ is a measure of particle size ($\gamma = \frac{a_p}{4a_b}$). The third parameter δ depends on the operating frequency and the viscosity of the liquid.

The definition of δ is given in Section 3.3 ($\delta = \sqrt{\frac{2\nu}{\omega}}/a_b$). All experiments are conducted at 20 kHz. The fluid used is pure water in one case ($\delta = 0.095$) and 24% glycerol water solution ($\delta = 0.130$) with dissolved Sodium polytungstate to vary fluid density (using Sodium polytungstate does not change the viscosity of the fluid). Particles with $a_p \leq 1 \mu\text{m}$ behave identically to fluid elements (their small size makes them behave passively). On the other end of the spectrum particles with $a_p > 10 \mu\text{m}$ should not be used in experiments as they start becoming comparable to the bubble radius and violate the condition $\gamma \ll 1$ which we have discussed in the Section 3.1

($a_b = 40 \mu\text{m}$). Experiments are conducted with $a_p = 2.5 \mu\text{m}$, $5 \mu\text{m}$ and $10 \mu\text{m}$ with $a_p = 1 \mu\text{m}$ used as passive particle proxies for streamlines. To vary $\hat{\kappa}$ we use two different particle densities ($\rho_p = 1.05 \text{ g/cm}^3$ and 1.19 g/cm^3).

The experiments are conducted at a constant inlet flow rate ($3 \mu\text{L/min}$). The input voltage of the piezo transducer is varied to change the value of streaming parameter s . It is noted that as discussed in the Section 2.4 we work with much larger values of s as opposed to the previous work [5,18]. The large value of s eliminates the presence of the upstream vortex. The reason for this choice of s is that we need the particle to be approach the bubble at a distance close enough to feel the effect of streaming near the bubble while not forcing the particle so close to the bubble that it experiences the repulsive short-range lubrication force. The small value of s from the previous work violates this criterion by forcing all particles to come very close to the bubble surface regardless of their initial position. It is seen from the results the closest approach distance of particle trajectory (h_{min}) is a parameter which greatly affects the behavior of a particle close to the bubble and its effect was not studied in the previous work (refer to Figure 4.4). To systematically study particle behavior with respect to this parameter we observe particles at different initial conditions (which ultimately translate to different values of h_{min}).

4.2 EXTRACTION OF STREAMLINE DATA

To conduct experiments, we use particles of the size $a_p = 1 \mu\text{m}$ to approximate streamlines. By tracking multiple trajectories of smaller particles (usually 4-5), it is possible to form an approximation of the ‘stream function’ (an example is shown in Figure 4.1). To do this

we assume that we have a stream function $\psi(x, y)$. A streamline is given by $\psi(x, y) = c$ where c is some constant.

Note that this stream function differs from the exact stream function (by a multiplicative and additive constant) as seen in theory. The usefulness of this function stems from the fact that an isoline of this function is a streamline. Thus, we can refer to each streamline by the constant denoted by $\psi(x, y)$. Using a gridded interpolant, we can obtain an approximation to the stream function using multiple particle trajectories. To do the interpolation we use griddata functionality in MATLAB (<https://www.mathworks.com/help/matlab/ref/griddata.html>), with triangulation based linear interpolation.

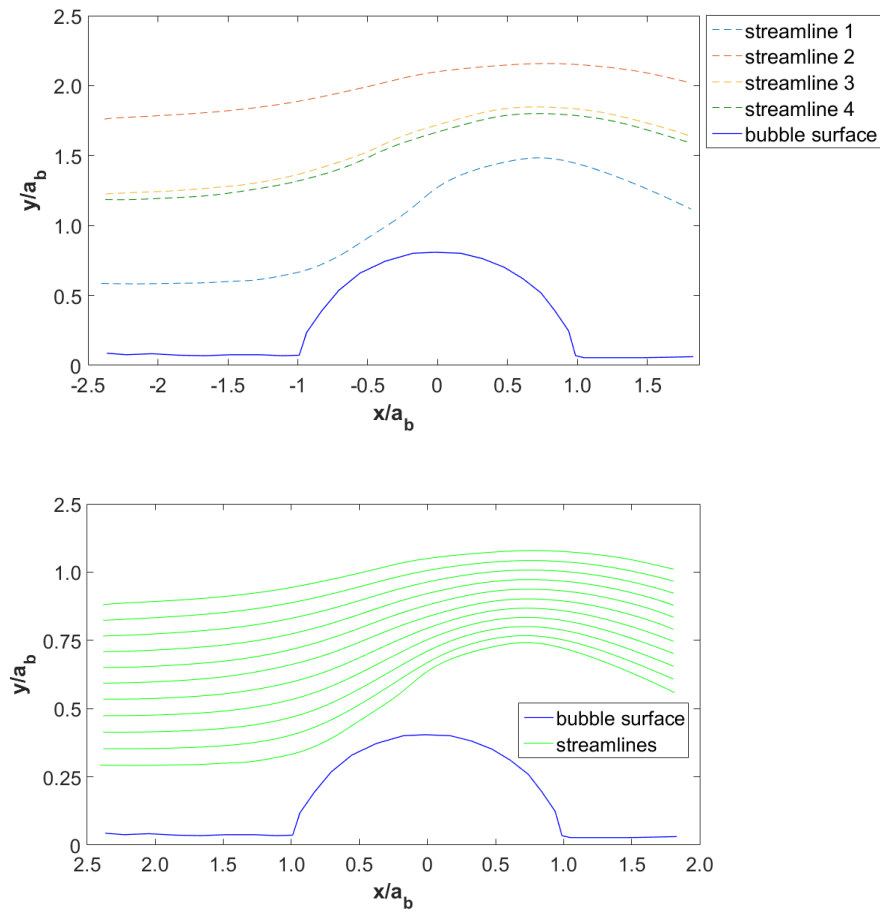


Figure 4. 1: a) raw particle trajectory data b)interpolated streamlines

To start the algorithm, we take the topmost (farthest from the bubble) and bottommost (closest to the bubble) particle trajectories and use the gridded interpolant to obtain an approximation of the stream function with these two trajectories as isolines. Naturally using only two trajectories would not give us a very accurate streamline picture. We need to add in the raw data present in a few more particle trajectories to get a more accurate approximation. We do this by a ‘prediction correction’ type of approach. The existing gridded interpolant is used to ‘predict’ the closest isoline for a particle trajectory. The interpolant is then ‘corrected’ by forcing the closest isoline to become the particle trajectory. The next step is to generate a new gridded interpolant like before but this time using three particle trajectories. The process is repeated with about 4-5 trajectories in total so we can then generate an image of the streamlines (in Figure 4.1 b).

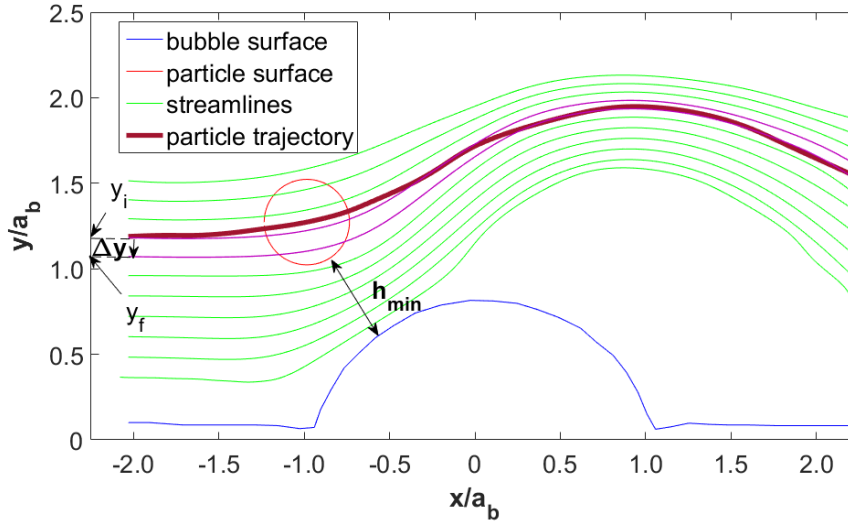


Figure 4.2 : $\delta = 0.095$, $\gamma = 0.0625$ and $\hat{\kappa} = 0.033$; $h_{min} \sim 20 \mu m$

4.3 ANALYSIS OF EXPERIMENTAL DATA

After obtaining the streamlines from the above process we can analyze the trajectory of the larger particle with respect to this. An example of this is seen in the Figure 4.2. Here we track a particle of size $a_p = 10 \mu m$. The flow runs from left to right. The dimensions in x and y direction are non dimensionalised with respect to bubble radius. We can see in this case that the

large particle does not follow the trajectory of the streamlines as seen by the purple streamlines that are made to bracket the large particle. In fact, as will become clearer the trajectory is first repelled from the bubble surface as it approaches. After it enters the latter part of the trajectory however it becomes attracted closer to the bubble.

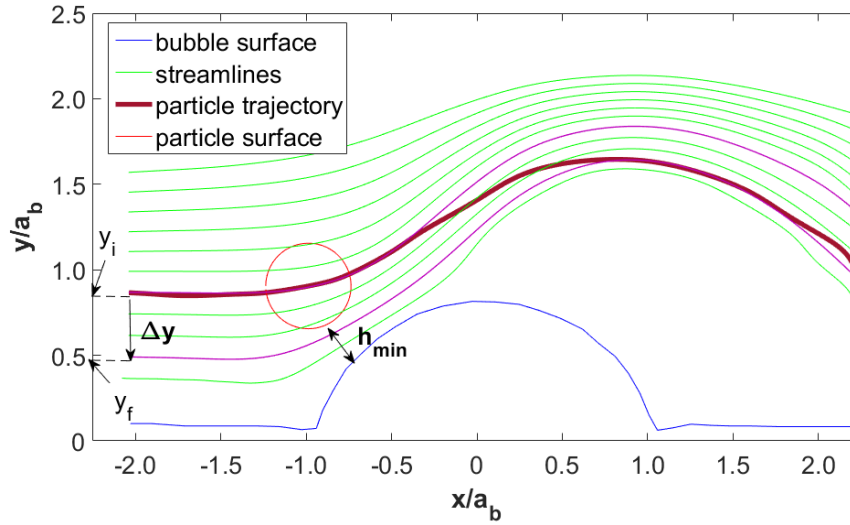


Figure 4.3: $\delta=0.095$, $\gamma = 0.0625$ and $\hat{\kappa}=0.033$; $h_{min} \sim 8 \mu m$

Figure 4.3 shows us an experimental case where all the parameters are the same as in Figure 4.2 except for the initial condition (equivalently h_{min}) of the particle. The effect of attraction is small in case of Figure 4.2 but it become significantly visible in case of Figure 4.3. The effect of changing particle trajectories is only significant when the particle is close to the bubble. This minimum distance between the surface of the particle and that of the closest approach is denoted as h_{min} . Ideally to get a measure of particle displacement we would look at the difference in y coordinate at $x = \infty$ and $x = -\infty$. This of course is not practically possible with a limited field of view available in experiment. To obtain a measure of displacement despite this we use the stream function that was derived from the previous section. We see that the particle only sees significant changes in trajectory when it is close to the bubble. From this we can infer that the particle will continue to follow the trajectory of the streamline on which it lies on the right side of the figure.

The particle is tracked upto $x = 2$ which is about $80\mu\text{m}$ downstream from the bubble. This is sufficiently far away from the downstream T-junction so as not to be affected by it. We can follow this streamline back to the beginning (ie the left-hand side). Note that this is very easily done since we have a description of the stream function as described in the previous section. Since the streamlines at this point are parallel the difference in the y coordinate at this point will give us a measure of the amount of displacement that a particle has undergone during its journey past the bubble. If the difference between the initial and final values ($\Delta y = y_f - y_i$ where y_f and y_i are final and initial y coordinates respectively) is negative this indicates ‘attractive’ behavior.

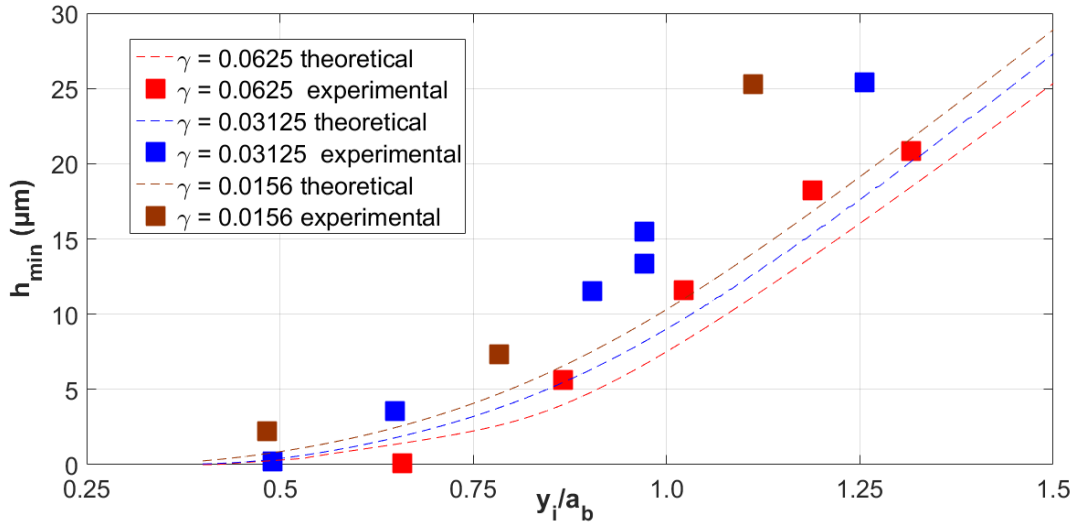


Figure 4.4: Variation of closest approach distance to initial y-coordinate for particle trajectories $\delta = 0.095$, $\hat{\kappa} = 0.033$, $s = 2$, Symbol size of the experimental data represents the magnitude of error in measurement.

Figure 4.4 shows us the variation of closest approach distance (h_{min}) with the initial y-coordinate (y_i) for a particle for a set of specified conditions both measured from experiment and calculated from theory. These theoretical calculations are arrived at by simulations of equations 3.17 and 3.18 and is further discussed in section 4.5. The justification of $s = 2$ is also discussed in Section 4.5. Note that all the experimental measurements have an error of $\pm 1\mu\text{m}$. This is due

to the primarily the measurement error in the particle size (for $a_p = 10\mu\text{m}$ there is an error of $0.3\mu\text{m}$) along with the error due to the optical set up (wavelength of incident light $\sim 0.7\mu\text{m}$) We see here that there is monotonic behavior and good agreement between experiment and theory. This behavior also gives us the justification to measure variation against just one of these variables. We choose to use closest approach distance as the parameter of interest because the magnitude of forces are more dependent on this quantity.

We note that as mentioned in Section 1.5 this method of analysis is quite different from what was last used by the group in [5,19]. There are two primary reasons for this. Firstly, in the previous work the flows studied have very strong streaming which ensures that the particles studied were very close to the bubble surface. In this regime, the particle experiences very strong forces in the radial direction and the particle velocity is largely in the azimuthal direction. This ‘uncoupled’ nature leads to a very good description in terms of a 1-D theory. Secondly, the object of the previous work was to measure the forces on these particles which requires us to use a measure of velocity perpendicular to the streamlines. In this work, we are utilizing very weak streaming which means that particles are not forced close to the bubble surface. We are also interested in the net displacement that the particle sees after crossing the bubble. For these reasons, the previous method does not fit our requirements.

4.4 EXPERIMENTAL RESULTS

In this Section, we comment on the different effects that are visible from experimental results. After this we will comment on trends that are visible in our experimental results.

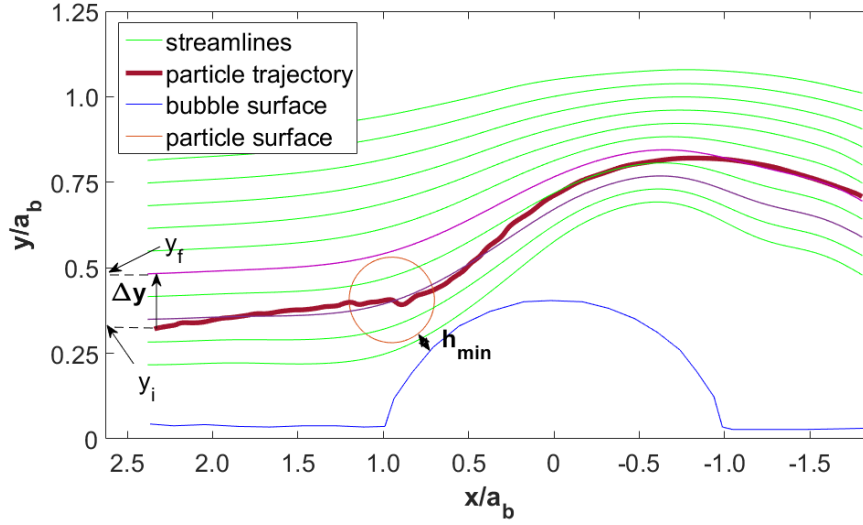


Figure 4.5: $\delta=0.130$, $\gamma = 0.0625$ and $\hat{\kappa}=0.047$; $h_{min} \sim 0.2 \mu m$

In the previous section we have used Figure 4.2 and 4.3 to describe the method by which we analyze the experimental data. These figures represent large particles ($\gamma = 0.0625$) which are denser than the suspended liquid ($\hat{\kappa} = 0.033$). As we expect from the theory prescribed in Section 3.2 we see the expected attractive behavior. Another result that is illustrated by these two cases is the effect of closest distance (h_{min}). As stated before the effect increases as we get closer to the bubble.

We now look at a different trajectory illustrated in Figure 4.5. Here we see if the particle gets very close to the surface of the bubble we get a net repulsive effect. We note that this is consistent with results that we see in earlier work [5,18]. This is easily explained by the purely repulsive short-range lubrication force. Particles that are far away from the bubble see no major effect. This trend is illustrated in Figure 4.6 which shows the variation of net displacement vs closest distance for this case. The shape of this graph is typical for all the experimentally studied cases. The only changes which occur are the presence/absence of an attractive regime and the magnitude of the displacement seen for different values of γ and $\hat{\kappa}$.

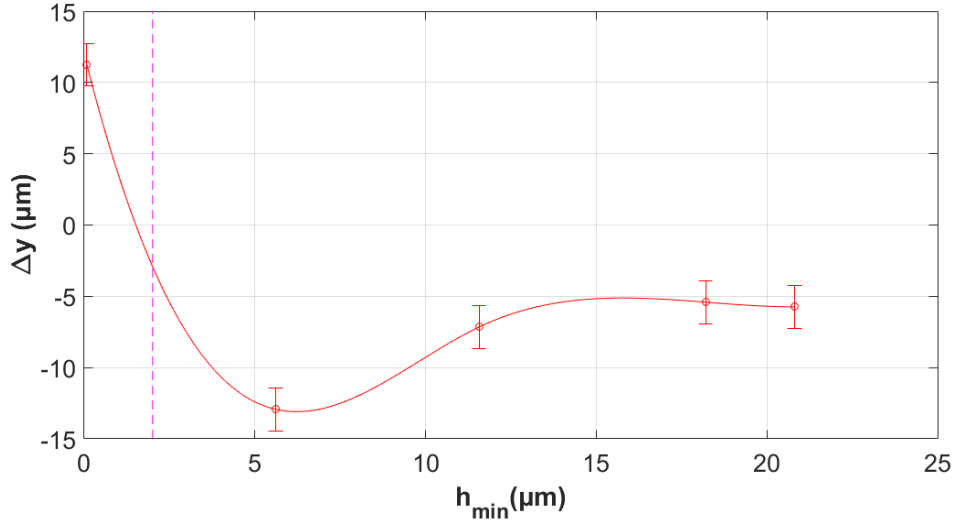


Figure 4.6: The typical variation of Δy vs h_{min} for experimental cases, $\delta=0.095, \hat{\kappa}=0.033, \gamma = 0.0625$

The pink line in Figure 4.6 at $h_{min} = 2.5\mu m$ indicates that the previous work [5,18] consisted of experimental cases where particles were restricted to values of $h_{min} < 2.5\mu m$ (due to low value of s as seen in Section 2.4) and often much less than this which explains why attractive forces were not seen.

Now that we have established the general behavior of Δy as a function of h_{min} we look at the variation we see with various values of $\hat{\kappa}$. An interesting result that is seen in experiment is seen in Figure 4.7. This figure shows a large density matched particle ($\hat{\kappa} = 0$). We see that there is an attractive effect here, showing that density mismatch is not an absolute necessity to see an attractive behavior (although as seen later it certainly increases the effect). This is not expected based on earlier work (since as seen in Figure 4.6 previous work does not deal with large values of h_{min}) but does match the predictions from theory in Section 3.2.

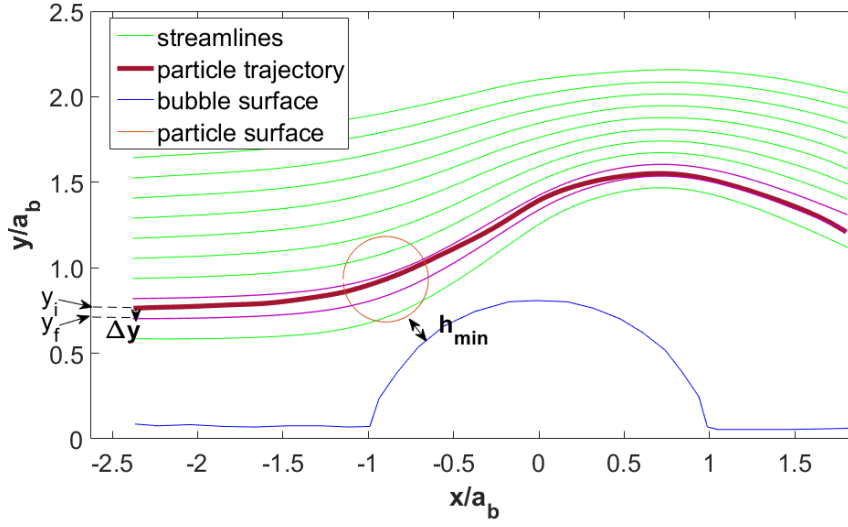


Figure 4.7: $\delta=0.130$, $\gamma = 0.0625$ and $\hat{\kappa}=0$; $h_{\min} \sim 5 \mu\text{m}$

Figure 4.8 summarizes the variation of attractive behavior as a function of $\hat{\kappa}$. This graph summarizes experiments with the same values of $\delta(0.130)$ and $\gamma(0.0625)$ and varying values of $\hat{\kappa}$ from -0.04 to 0.047 . We note that the shape of these curves is similar to Figure 4.6. It is seen from this graph that the increase of $\hat{\kappa}$ causes an increase in the amount of attraction felt by the particle. At $\hat{\kappa} = -0.04$ we see that the entire attractive region of the graph is absent showing that for this region of parameters there is no attraction. It is noted that according to Figure 3.1 a) $\gamma = 0.0625$ and $\hat{\kappa} = -0.04$ falls very close to the repulsive region. We can see that the small variation in $\hat{\kappa}$ can certainly make large changes in the attractive behavior seen by a particle. Lastly, we see the effect of the variation in particle size γ . First, we see the trajectory of a smaller particle in Figure 4.9. Here we see that the effect on a smaller particle is much smaller than when we have a large particle.

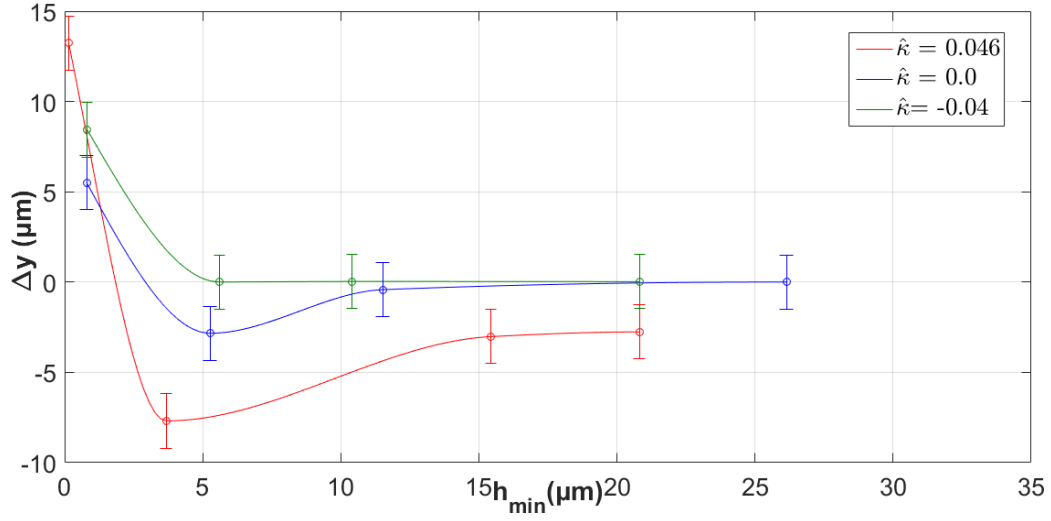


Figure 4.8: Plot of displacement vs closest distance for $\gamma = 0.0625$

This is seen by comparing Figure 4.9 and Figure 4.3 where for a similar set of parameters (except γ) we see effects that are very different in magnitude.

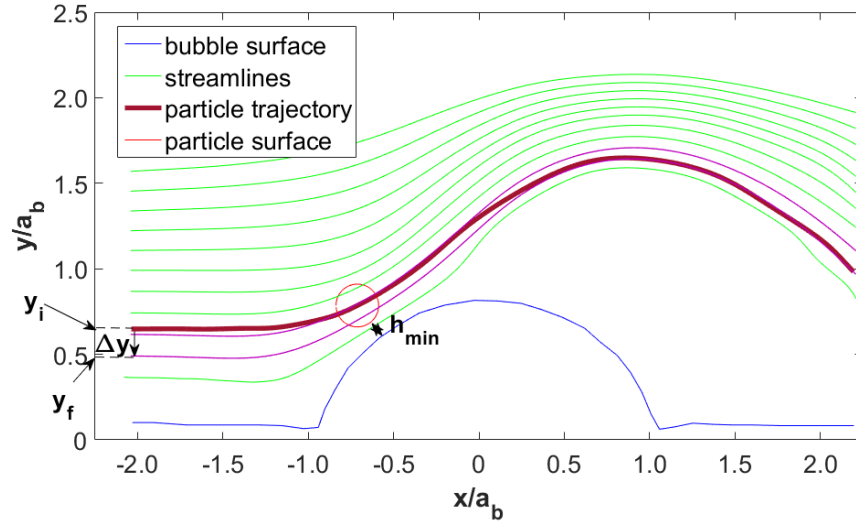


Figure 4.9 $\delta=0.095$, $\gamma = 0.03125$ and $\kappa=0.033$; $h_{min} \sim 4 \mu m$

We can see these effects from Figure 4.10. As seen in this figure particles that have a larger value of γ i.e. larger particles see increased effects. We see that for particles with $\gamma = 0.0156$ ($a_p = 2.5 \mu m$) we find net displacements no larger than a micron. Note that this justifies our choice of particles with $a_p = 1 \mu m$ as proxies for streamlines since these particles according to the above

trend will show no change in particle trajectory. And as we expect we see that attractive effects are stronger for particles with larger values of γ and that low values of γ simply tend to weaken all effects. In Figure 4.10 b) we see that the attractive behavior is seen only in particles of larger size ($\gamma = 0.0625$) and not in particles of smaller size ($\gamma < 0.03125$). The experiment at $\gamma = 0.0156$ and $\hat{\kappa} = 0.033$ lies well within the repulsive region. However since the particle is very small one does not see any significant change in trajectory.

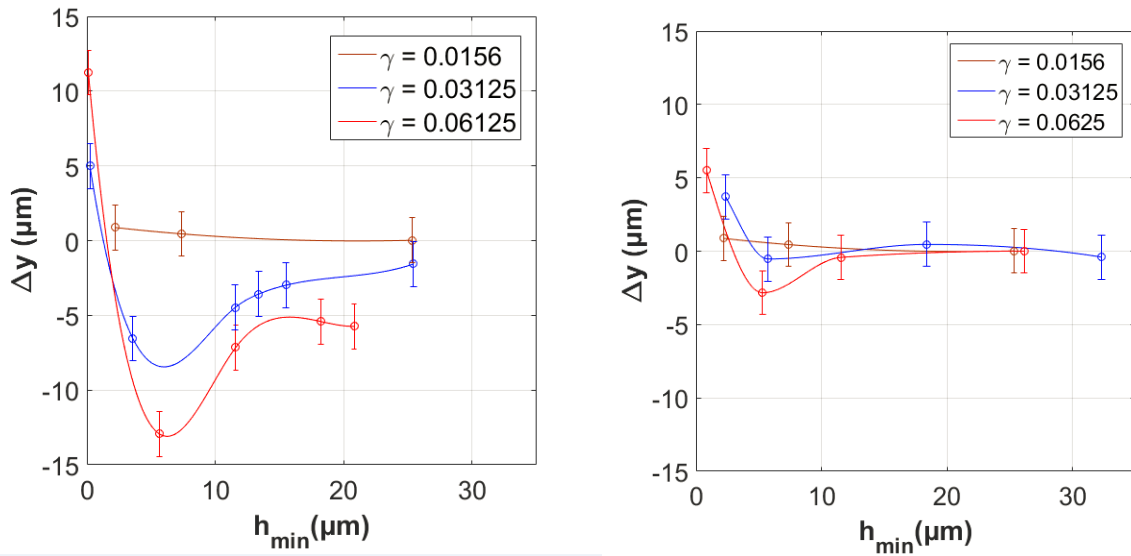


Figure 4.10: Plots of displacement vs closest distance for a) $\hat{\kappa}=0.033$ $\delta = 0.095$ b) $\hat{\kappa}=0$ $\delta = 0.130$

This result along with the conclusions we can draw from Figure 4.8 show that large particles which are denser than the suspended fluids see significant attraction. Figures 4.8 and 4.10 also show the general trend that particles which are too close get repelled and particles which are very far away see no significant effect.

4.5 THEORETICAL RESULTS

In the previous section we saw many trends that are experimentally obtained. It is then worth asking what the theory discussed in chapter 3 says about these trends. First, we can look at the Figure 3.1 to see where our experiments lie on this phase plot. Most of our experiments lie in the attractive region of the plot. We observe that those experiments that lie in the repulsive

region ($[\gamma = 0.0625, \hat{\kappa} = -0.04, \delta = 0.095]$ and $[\gamma = 0.0156, \hat{\kappa} = 0.033, \delta = 0.130]$) show no attractive behavior. Those that are in the attractive region show some attractive behavior. Thus, there is complete agreement with the theoretical predictions of the 1-D theory which justifies its use as a qualitative predictor.

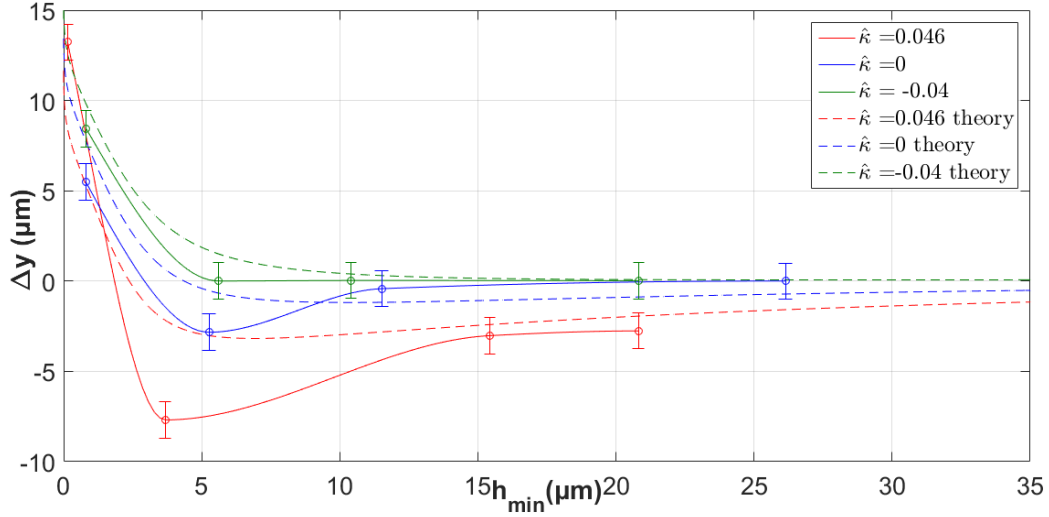


Figure 4.11: Plot of displacement vs closest distance for $\gamma = 0.0625$, Comparison of theory and experiments

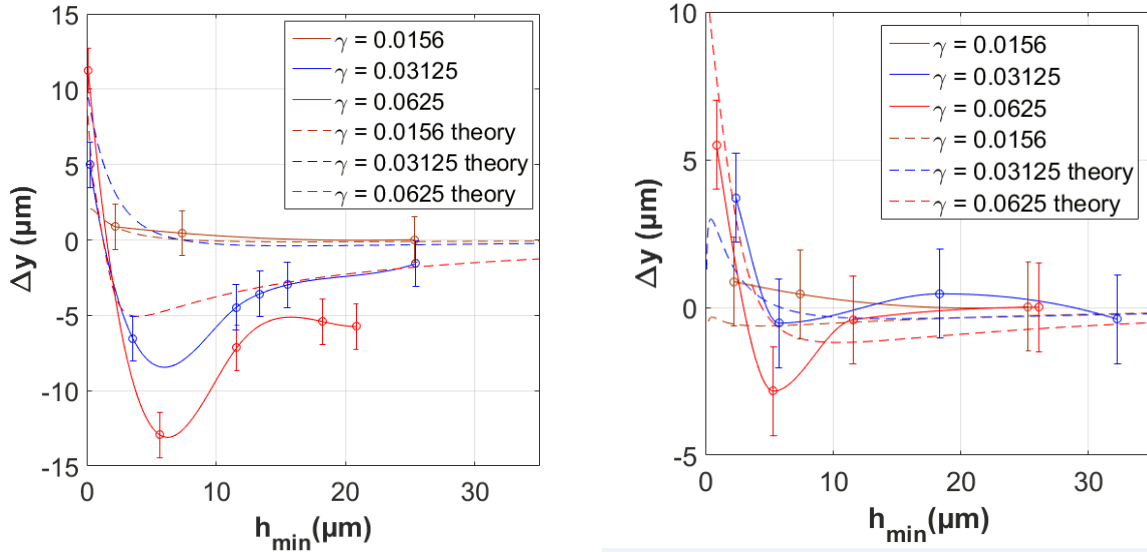


Figure 4.12: Plots of displacement vs closest distance for a) $\hat{\kappa}=0.033$ b) $\hat{\kappa}=0$, comparison of theory and experiments

For more quantitative theoretical predictions we look particularly at the ‘slow time’ theory that is prescribed in Section 3.3. We can use equations 3.17 and 3.18 to simulate particle trajectories

which we can then use to measure quantities such as net displacement and closest distance. In order to run these simulations, we need to assume a value for s so as to obtain the details of the velocity fields. We compare streamline pictures that are obtained theoretically with those obtained experimentally (for example comparing Figure 3.3 and Figure 4.1 b). In these two Figures, we compare the density of the bundle of streamlines at positions which would be significantly under the influence of the two vortices in the absence of the transport flow ($r \sim 1.2$, $\theta \sim \frac{3\pi}{4}$ and $x = 2$). We also look to Figure 4.4 to see that when we simulate with $s = 2$, we obtain theoretical curves that are a good match for values seen in experiments. The above results allow us to justify the assumed value of $s = 2$. Figure 4.11 and Figure 4.12 show the comparison between what we see in experiments to what is predicted in theory using the numerically obtained solutions to equations 3.17 and 3.18.

The theoretical predictions shown in both Figure 4.11 and Figure 4.12 show the same qualitative behavior that matches with the general behavior from experiments (shown in Figure 4.6). We see that the particles are expected to see repulsion close to the surface of the bubble and as we go further off we see net attraction (for large dense particles) and then the displacement asymptotes to 0. Another consistent trend is that density mismatch increases the attractive forces seen by particles (as seen in Figure 4.11). Finally, we see that the theory predicts that small particles ($\gamma = 0.0156$) also do not experience any major changes from fluid trajectories (Figure 4.12).

The first inaccuracy we see in the theory is that the asymptotes decay very slowly which is not the case in experiments. The second inaccuracy we see is that the theory consistently underpredicts the expected displacement. It has been discussed at the end of Section 3.3 the current version of the ‘slow time’ theory can be further refined by including a few terms present in the 1-

D theory. The absence of these terms in the ‘slow time’ theory can possibly explain the inaccuracies seen above.

As stated at the end of Section 3.3 we can simulate equation 3.9, which includes the terms that are not present in the 2-D slow time theory, and solve the equations on the oscillatory time scale. In the Figure 4.13 we show results of these full Maxey Riley simulations and how they compare with the slow time theory as well as experimental predictions for one particular case. It is important to note here that the solutions to the full MR equations are dependent on the value of ϵ which is not the case in the slow time theory (in the slow time theory we assume that ϵ is small). To find a value of ϵ for these simulations match the amplitude of the bubble oscillation to that practically seen in experiments ($\sim 2 \mu\text{m}$). It is worth noting that the data from these simulations would be more accurate than one produced by an equivalent slow time theory since it takes into consideration the finite amplitude in oscillation of the surface to surface distance.

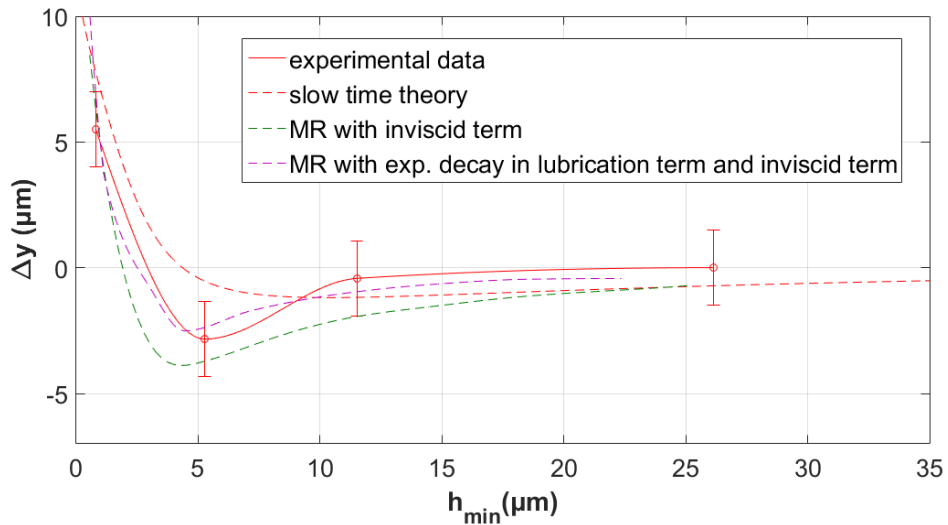


Figure 4.13 : Comparison of several versions of solutions of the Maxey Riley equations (MR) and how they compare with the slow time theory; $\gamma = 0.0625, \hat{\kappa} = 0.0, \delta = 0.130$

We first look at the solution with the addition of only the inviscid correction term (green). This term serves to make the attractive region much stronger thus correcting for the second inaccuracy

i.e. underestimation of attraction. The problem with this version of the theory is that it overcorrects the previously too-weak attraction. The solution to the MR equation including both the inviscid correction and the exponential decay in the lubrication term (violet) seems to have a very good correlation with the experimental data. It does well by predicting the correct magnitude of attraction in this case. It also places the value for minimum Δy at a point which is very close to what we see in experiments. Once a slow time theory analogous to equations 3.17 and 3.18 is developed, including both the inviscid term and the exponential decay in the lubrication term a better comparison with experiments over a wider range of approach distances is expected to be possible.

CHAPTER 5: CONCLUSIONS

5.1 CONCLUSIONS

In this piece of work, we have studied the variation in the trajectory of microparticles as they move in a flow field which is a superposition of a Poiseuille flow and a 2-D microbubble streaming flow. In previous work it was shown that density matched particles that approached the interface of the oscillating bubble within a distance of few microns are repelled from the bubble, hence traversing streamlines ending up in the Poiseuille flow higher than they initially started. Theoretical predictions however show that certain particles particularly those that are non-density matched particles can potentially be attracted to the bubble interface. Therefore, we start by investigating particles which are non-density matched.

It is seen that we can modify the previous experiments by lowering the strength of the streaming flow. This allows us to experiment with a larger variety of particle trajectories compared to that which was studied in the previous work. A novel addition in this work is the study of particle behavior with the variation in the minimum surface to surface distance between the particle surface and the interface as it follows a trajectory past the bubble (quantity denoted by h_{min}). We conduct a systematic study of particle behavior with respect to density mismatch, particle size and fluid viscosity.

Experimental results find a generic behavior of a particles a function of h_{min} . For very close approach distances they show the same kind of repulsive behavior as previous experiments. If the value of h_{min} is on the order of particle size it is possible to see significant attraction depending on the value of the control parameters. This attraction diminishes to 0 as the h_{min} value becomes larger, i.e. the particle does not get close to the bubble interface.

The parameter variation study shows that the most attraction is seen by particles which are denser than the fluid and large. As one moves from heavier to lighter particles the amount of attraction that we see diminishes and is ultimately lost, making the particle repelled for all values of h_{min} . The same can be said of moving from larger to smaller particles at a fixed density.

We see that these results are qualitatively consistent with a purely radial approximation to the Maxey Riley equation for which, on performing time scale separation and then obtaining a solution, a phase diagram can be easily obtained. In order to obtain a better theoretic description of the particle behavior based on the different trajectories we introduce an analogous 2-D version of the Maxey Riley equation. The ‘slow time’ solution to these equations are used to obtain quantitative predictions on the behavior of particles in experiments. We see that this version of the 2-D theory captures the general trend based on the variation with h_{min} discussed earlier and shows good qualitative and semi-quantitative agreement with the experimental data.

Possible applications of this work can be in the design of microfluidic devices in bio-engineering where we may wish to manipulate small cells based on differences in their properties such as density. The theory also predicts that one can potentially design devices or flow fields to trap particles (not possible in our experimental scenario). Another advantage of the current system is that the behavior of the device can be dynamically changed by varying the amplitude and frequency of the driving oscillation.

Possible future work in this area includes the refinement of the 2-D Maxey Riley equations to closer match the experimental results. Further experiments can be conducted to study the variation with respect to driving frequency of the microbubble as well as the viscosity of the suspended fluid. The rich possibilities of influencing particle behavior not only by the particle and fluid properties, but by the geometry and pattern of the flow field opens up more

sophisticated particle migration and sorting capabilities than have been possible in traditional inertial microfluidics.

REFERENCES

- [1] N Riley. Steady streaming. *Annual Review of Fluid Mechanics*, 33(1): 43–65, 2001.
- [2] Michael S Longuet-Higgins. Viscous streaming from an oscillating spherical bubble. In *Proceedings of the Royal Society of London A: Mathematical, Physical and Engineering Sciences*, volume 454, pages 725–742. The Royal Society, 1998.
- [3] Cheng Wang, Shreyas V Jalikop, and Sascha Hilgenfeldt. Efficient manipulation of microparticles in bubble streaming flows. *Biomicrofluidics*, 6(1):012801, 2012.
- [4] Cheng Wang, Shreyas V Jalikop, and Sascha Hilgenfeldt. Size-sensitive sorting of microparticles through control of flow geometry. *Applied Physics Letters*, 99(3):034101, 2011.
- [5] Raqeeb Thameem, Bhargav Rallabandi, and Sascha Hilgenfeldt. Particle migration and sorting in microbubble streaming flows. *Biomicrofluidics*, 10(1):014124, 2016.
- [6] Robin H Liu, Jianing Yang, Maciej Z Pindera, Mahesh Athavale, and Piotr Grodzinski. Bubble-induced acoustic micromixing. *Lab on a Chip*, 2(3):151–157, 2002.
- [7] Cheng Wang, Bhargav Rallabandi, and Sascha Hilgenfeldt. Frequency dependence and frequency control of microbubble streaming flows. *Physics of Fluids (1994-present)*, 25(2):022002, 2013.
- [8] Lin Guo. A numerical study on microbubble mixer. 2014.
- [9] Philippe Marmottant and Sascha Hilgenfeldt. Controlled vesicle deformation and lysis by single oscillating bubbles. *Nature*, 423(6936):153–156, 2003.
- [10] B. Rallabandi, C. Wang, and S. Hilgenfeldt. Two-dimensional streaming flows driven by sessile semicylindrical microbubbles. *J. Fluid Mech.*, 739: 57–71, 2014.
- [11] B. Rallabandi, A. G. Marín, M. Rossi, S. Hilgenfeldt, and C. J. Kähler. Three-dimensional streaming flow in confined geometries. *J. Fluid Mech.*, 777:408-429, 2015
- [12] Alvaro Marin, Massimiliano Rossi, Bhargav Rallabandi, Cheng Wang, Sascha Hilgenfeldt, and Christian J Kähler. Three-dimensional phenomena in microbubble acoustic streaming. *Phys. Rev. Appl.*, 3(4):041001, 2015.
- [13] M. S. Longuet-Higgins. Mass transport in water waves. *Phil. Trans. Roy. Soc. Lond. Series A: Mathematical and Physical Sciences*, 245(903): 535–581, 1953.
- [14] N. Riley. Steady streaming. *Annu. Rev. Fluid Mech.*, 33:43–65, 2001.
- [15] H. Bruus. *Theoretical Microfluidics*. Oxford Master Series in Physics. OUP Oxford, 2008.

- [16] Martin R Maxey and James J Riley. Equation of motion for a small rigid sphere in a nonuniform flow. *Phys. Fluids*, 26(4):883–889, 1983.
- [17] Efstathios E Michaelides. Review the transient equation of motion for particles, bubbles, and droplets. *Journal of fluids engineering*, 119(2): 233–247, 1997.
- [18] Thameem Raqeeb, Sorting of particles in bubble streaming flows. Master’s Thesis, University of Illinois at Urbana Champaign.
- [19] Thameem Raqeeb, Rallabandi Bhargav, Hilgenfeldt Sascha. Fast inertial particle manipulation in oscillating flows. *Phys Rev Fluids*. 2 .052001 (2017)
- [20] Rallabandi Bhargav, Wang Cheng, Hilgenfeldt Sascha. Analysis of optimal mixing in open-flow mixers with time-modulated vortex arrays. *Physical Review Fluids*. 2. 10.1103 (2017)
- [21] Maali Abdelhamid, Boisdard Rodolphe, Chraïbi Hamza Zhang Zaicheng, Kellay Hamid, Würger Alois. Viscoelastic Drag Forces and Crossover from No-Slip to Slip Boundary Conditions for Flow near Air-Water Interfaces. *Physical Review Letters*. 118. 10.1103 (2017)
- [22] Agarwal Siddhansh, Hilgenfeldt Sascha, Rallabandi Bhargav. *Inertial Forces for Particle Manipulation near Oscillating Interfaces*. Preprint, 2018
- [23] Chen Yun, Fang Zecong, Merritt Brett, Strack Dillon, Xu, Jie, Lee Sungyon. Onset of Particle Trapping and Release via Acoustic Bubbles. *Lab Chip*. 16. 10.1039. (2016)